Chemical Engineering Journal 474 (2023) 145992

Contents lists available at ScienceDirect

Chemical Engineering Journal

journal homepage: www.elsevier.com/locate/cej

Synchronous regulation of Schottky/p-n dual junction in Prussian blue-derived Janus heterostructures: A path to ultrafast long life potassium ion batteries

Shou-Shan Mai [a], Kai-Yuan Hsiao [b], Yi-Chun Yang [a], Ying-Rui Lu [c], Ming-Yen Lu [b], Yi-Yen Hsieh [a], Che-Bin Chang [a], Hsing-Yu Tuan [a,*]

[a] Department of Chemical Engineering, National Tsing Hua University, Hsinchu 30013, Taiwan
[b] Department of Materials Science and Engineering, National Tsing Hua University, Hsinchu 30013, Taiwan
[c] National Synchrotron Radiation Research Center, 300 Hsinchu, Taiwan

ARTICLE INFO

Keywords:
Janus heterostructure
P-n junction
Schottky junction
Graphite layer
Potassium ion battery

ABSTRACT

Practical applications of conversion-type metal selenide electrodes in potassium ion batteries (PIBs) encounter multiple challenges, such as particle aggregation, the shuttle effect, and pulverization during cycling. We design a Janus heterostructure, namely $CoSe_2$-$FeSe_2$/graphite/N-doped carbon (CFS//g@NC), with dual heterojunctions (p-n and Schottky junction), which generates the synergistic effect to enhance interface charge storage and improve electrode structure integrity. When the Janus heterostructure is used as a PIB anode, it demonstrates high-rate performance up to 10 A/g, offering a capacity of 200 mA h g^{-1} and excellent cycling stability of over 2500 cycles at 0.5 A/g. According to the density functional theory (DFT) calculations, the diffusion barrier of K ions on CFS//g@NC is two times lower than that on $CoSe_2$ or $FeSe_2$. The distribution of n-type and p-type semiconductors in the Janus particles has been confirmed by quantitative assessment through dark-field electron microscopy. In addition to the p-n junction crossing two semiconductor interfaces, the Schottky junction between the graphite layer derived from Prussian blue analogues (PBA) and the semiconductor also creates a built-in electric field, thus enhancing ion/electron transport and increasing the diffusion of potassium ions. This work provides new insights into the architectural strategy of multi-layer heterointerfaces and offers a promising new pathway for anode design in PIBs.

1. Introduction

Rechargeable potassium ion batteries (PIBs) have attracted considerable attention due to their abundant potassium resources, high energy density, rapid ion transport kinetics in electrolytes, and cost-effectiveness. The standard redox potential of K^+/K (−2.93 V) is higher than that of Li^+/Li (−3.04 V), paving the way for their utilization in practical full cells, which demand high working voltage and superior energy density [1,2]. The weak Lewis acidity of potassium ions facilitates their diffusion across a variety of electrolytes, thereby effectively reducing interfacial polarization between the electrolytes and electrodes. However, challenges persist in the development and deployment of PIBs. The large atomic radius of potassium atoms results in substantial volume expansion during charge/discharge cycles, compromising the integrity of the electrode and causing a sharp decline in both specific capacity and energy density [3]. Moreover, potassium metal is more reactive than lithium metal, making it more prone to react with electrolytes and form dendrites, resulting in poor electrochemical performance and even posing significant safety hazards. Consequently, the rational design of electrode materials to achieve satisfactory electrochemical performance is a major challenge in the field of energy storage devices [4–7].

Presently, anodes in PIBs can be classified into three categories: intercalation, alloying, and conversion types [8]. Metal sulfides (MS) and metal selenides (MSe), both of which are involved in conversion and alloying reactions for PIB anodes, exhibit a higher theoretical capacity than graphite intercalation anodes [9,10]. Comparing the two, MSe demonstrates superior electronic conductivity. It has an electrical conductivity of 1×10^{-3} S m^{-1}, markedly higher than MS's conductivity of 5×10^{-28} S m^{-1} [11]. Consequently, MSe exhibits lower energy barriers

* Corresponding author.
E-mail address: hytuan@che.nthu.edu.tw (H.-Y. Tuan).

https://doi.org/10.1016/j.cej.2023.145992
Received 2 June 2023; Received in revised form 2 August 2023; Accepted 8 September 2023
Available online 9 September 2023

for ion diffusion compared to MS. MSe is notable for its weaker M−Se bonds compared to MS, which could potentially heighten its reaction activity [12]. Nevertheless, MSe encounters substantial hurdles, including severe pulverization owing to volume expansion and the shuttle effects that occur during charge and discharge cycles [13]. To address these issues, Liu et al. constructed dual phosphorus doped Fe_3Se_4/three-dimensional (3D) graphene anode for PIBs, which exhibits superior rate capability and long cycling lifespan due to the dual P doping interface and 3D graphene [14]. Lin et al. designed the double protection of C layer and graphene to buffer the huge volume variation of α-MnSe nanorods, further boost outstanding electrochemical performance. These results show that the carbon layer can effectively relieve volume expansion of MSe [15].

Heterogeneous hybrid materials, due to their abundant boundary areas, can significantly reduce capacity decay for MSe anodes, complementing carbon coating methods and the beneficial effects of synergistic reactions. The confluence of different semiconductor types in heterostructures spontaneously generates an inherent built-in electric field at the interface, presenting a promising approach to influence electrochemical reactions. In recent years, heterostructure materials have seen diverse applications and developments, spanning fields from field-effect transistors (FETs) to photovoltaics. Effects originating from heterostructure interfaces result in performance characteristics that are distinct from those of the previously used materials. For instance, Lee et al. designed graphene (Gr)-bridged heterostructures for FETs with non-classical transfer characteristics, reducing the potential barrier between semiconductors via Gr-bridging [16]. Zhang et al. demonstrated that the absorption efficiency of near-infrared light in topological crystalline insulator heterostructures was enhanced and the separation of photogenerated carriers significantly facilitated through a built-in electric field, leading to the fabrication of a high-performance, self-driven photodetector [17]. On the other hand, Zhang et al. explored bromine vacancy defects in $CsSnBr_3/SnS_2$ heterostructures and identified a bandgap narrowing caused by interfacial electronic states, thereby enhancing the photovoltaic performance of $CsSnBr_3$ [18]. Meanwhile, heterostructure materials have been extensively utilized in electrochemical energy storage due to their unique interfaces, robust structures, and synergistic effects. Constructed by coupling components with varying bandgaps, heterostructure materials, aided by the creation of interfacial internal electric fields, can expedite charge transfer and augment reaction kinetics during discharge/charge processes, thereby substantially enhancing rate performance and cycling performance [19–21]. Various types of heterostructures, including p-n junctions and Schottky junctions, have been examined for their impact on electrochemical performance. Hsieh et al. designed a 1D/2D van der Waals heterostructure with a p-n heterojunction, exhibiting high-rate capability and exceptional cycling stability in PIBs through crosslinked wire-contact phase boundaries [22]. Chu et al. created a multiheterostructure consisting of a double carbon layer and a Schottky junction, which effectively buffered volume changes, maintained structural stability, and enhanced electron transport rates, resulting in excellent electrochemical performance in PIBs [23].

The generation of combined p-n and Schottky heterojunctions may promise to redistribute interfacial charge storage and improve electrode structural integrity. Despite this, evidence demonstrating increased electrochemical storage as a result of the synergistic function of these two heterostructures remains limited. In this study, we adopt a $CoSe_2$-$FeSe_2$/graphite/N-doping carbon (CFS//g@NC) Janus heterostructure design with both of p-n and Schottky junctions to achieve efficient potassium storage. The p-n junctions formed between p-type $FeSe_2$ and n-type $CoSe_2$. A few nanometer-thick of graphite layer wrapped the $CoSe_2$-$FeSe_2$ Janus nanoparticles formed the Schottky junctions, which attracts and traps the potassium ions. As a result, both of p-n and Schottky junction form the built-in electric field, improving the diffusion of potassium ion and accelerating charge transfer. Constructing dual junction and carbon layer has become an important consideration in improving the performance of PIB. The CFS//g@NC displays superior potassium storage performance with high cycling stability over 2500 cycles and high rate performance (10 A g^{-1}). Besides, Kelvin probe force microscopy (KPFM) analysis and density functional theory (DFT) calculations confirm the fast ion transport in CFS//g@NC. This study proposes a strategy to construct the heterostructure materials with multilayered structure for the energy storage fields.

2. Experimental section

2.1. Materials

Cobalt(II) chloride hexahydrate ($CoCl_2{\cdot}6H_2O$,≧98%), Iron(III) chloride hexahydrate ($FeCl_2{\cdot}6H_2O$≧98%), potassium citrate tribasic monohydrate ($C_6H_5O_7K_3{\cdot}2H_2O$), potassium ferricyanide(III) ($K_3[Fe(CN)_6]$ ≧99%), Potassium hexacyanocobaltate(III) ($K_3[Co(CN)_6]$≧90%), ethanol (ACS reagent grade,≧99.5%), 2-Amino-2-(hydroxymethyl)-1,3-propanediol ($NH_2C(CH_2OH)_3$, ACS reagent grade,≧99.8%), Dopamine hydrochloride($(HO)_2C_6H_3CH_2CH_2NH_2{\cdot}HCl$), Iron powder (J.T. Baker), Cobalt powder (J.T. Baker), Selenium (powder, −325 mesh, 99.5%), dimethyl carbonate (DMC, anhydrous 99%), and potassium metal (chunks in mineral oil, 98%) were purchased from Sigma-Aldrich. Potassium bis(fluorosulfonyl)imide (KFSI, 97%) was purchased from Combi-Blocks. Sodium carboxymethyl cellulose (NaCMC, average $M_w \sim$ 700,000), Super-P and coin-type cell CR2032 were purchased from shining energy. Glass fiber was purchased from Advantec. Copper and aluminium foil were purchased from Chang-Chun group.

2.2. Synthesis of Co/Fe-Prussian blue analogues (PBA)

Typically, bimetallic Co/Fe-PBA polyhedrons were synthesized by a co-precipitation method at room temperature. 3 mmol of $CoCl_2{\cdot}6H_2O$ and 3 mmol of $C_6H_5O_7K_3{\cdot}2H_2O$ were dissolved in 50 mL deionized water to prepare solution A, and 1 mmol of $K_3[Fe(CN)_6]$ was dissolved in 50 mL deionized water to prepare solution B. Then, solution B was added to solution A slowly under magnetic stirring for 1 h and aging for 24 h. Finally, Co/Fe-PBA was obtained by centrifugation and wash with deionized water and ethanol several times, followed by drying overnight at 60 °C.

2.3. Synthesis of Co/Fe-PBA@PDA

Firstly, 100 mg Co/Fe-PBA nanocubes and 50 mg dopamine hydrochloride were ultrasonically added in a Tris-buffer solution (0.1 M, 100 mL) for 30 mins and magnetic stirring for 3 h. The products were collected by centrifugation 4 times using DI water and ethanol (1:1), then dried at 60 °C overnight.

2.4. Synthesis of CFS//g@NC

The Co/Fe-PBA@PDA were pyrolyzed at 600 °C for 2 h with a heating rate of 5 °C min^{-1} at Ar atmosphere in a vacuum quartz tube furnace, Co-Fe//g@NC were obtained. Se powder and Co-Fe//g@NC with the mass ratio of 3:1 were put in quartz boat. The selenization process was performed at 400 °C for 4 h after pyrolysis process in furnace at Ar atmosphere. After selenization process, CFS//g@NC were obtained. For comparison, the $CoSe_2$//g@NC and $FeSe_2$//g@NC were synthesized by a similar method.

2.5. Material characterization

All material's morphologies were investigated using scanning electron microscopy (SEM, HITACHI-SU8010) with 10 kV accelerating voltage, transmission electron microscopy (TEM, JEOL, JEM-ARM200FT, serviced provided by NTHU) with an accelerating voltage of 200 kV for investigating structural analysis including morphology,

crystal lattice spacing, high-angle annular dark-field (HAADF) and selected-area electron diffraction (SAED), high-resolution X-ray photoelectron spectroscopy (XPS, ULVAC-PH, PHI QuanteraII, NTHU). All the spectra obtained from XPS analysis were first calibrated by referencing the standard binding energy of C 1s (284.8 eV), followed by the curve fitting using the software of XPSPEAK VER. 4.1. X-ray diffraction (XRD, Bruker D8 ADVANCE) with Cu-Ka radiation (λ = 1.54 Å). The ultraviolet photoelectron spectroscopy (UPS, ULVAC PHI 5000 Versa Probe, serviced provided by NTU) and UV–vis (Aglient, serviced provided by NTNU) spectra are used for confirming the valence band and energy gap. The electron paramagnetic resonance (EPR) (BRUKER, ELEXSYS E-580, serviced provided by NTHU) with frequency of 6000 GHz. The KPFM (Bruker, Model: Dimension ICON, serviced provided by NTHU) are used for measure surface charge density. Thermogravimetric analysis (TGA) was obtained using a thermogravimetric analyzer (TA, Q50) in an air flow at a heating rate of 10 °C min^{-1} from ambient temperature to 800 °C. Surface area was detected by Brunauer–Emmett–Teller (BET) method. The K-edge X-ray absorption spectroscopy (XANES) of CFS//g were measured in fluorescent mode at the beamline of TPS 44A at the National Synchrotron Radiation Research Center (NSRRC) in Taiwan. All the XANES data were analyzed by Athena software (version 0.9.26) [24].

2.6. Electrochemical measurements

The anode electrode was prepared by mixing active material, super P, NaCMC in the ratio of 7:2:1 in distilled water to form a homogeneous slurry. The slurry was coated on the copper foil by doctor blade and dried at 80 °C under argon atmosphere. The average material mass loading of each electrode was 0.8 ~ 1.1 mg cm^{-2}. For electrochemical testing, the coin-type half-cell (CR2032) was assembled in an argon filled glovebox. For the half-cell, potassium metal foil is used as the counter electrode, glass fiber and Celgard 2400 membrane were used as the separator, a solution of 1 M KFSI in DMC as electrolyte. The galvanostatic discharge/charge tests were carried out in the voltage range of 0.01 V to 3 V by Neware battery test system. Before the stability test at 500 mA g^{-1}, the battery was cycled three times at 50 mA g^{-1}. Cyclic voltammetry (CV) and electrochemical impedance spectroscopy (EIS) was collected by multi-channel electrochemical analyzer (Bio-Logic-science Instruments, VMP3) with a potential window of 0.01–3.00 V and a frequency of 600 kHz to 50 mHz. The galvanostatic intermittent titration technique (GITT) was charged/discharged at a current density of 50 mA g^{-1} for 10 min with a relaxation time of 1 h.

2.7. Mott-Schottky test

Mott–Schottky plots were also measured with a 3-electrode setup in 0.1 M KOH electrolyte on an electrochemical workstation (Bio-Logic-science Instruments, VMP3). CFS//g@NC, $FeSe_2$//g@NC and $CoSe_2$//g@NC was coated on glassy carbon electrode as the working electrode, along with a s Ag reference electrode and Pt wire counter electrode.

2.8. DFT calculation

The calculations were performed with DFT implemented in the Vienna *ab initio* simulation package VASP [25]. The projected augmented wave (PAW) method was used to describe ion core-electron interactions and the exchange-functional correlation was treated by the generalized gradient approximation (GGA) of Perdew-Burke-Ernzerhof (PBE) functional [26]. The van der Waals interaction is described by the DFT-D3 approach [27]. The cutoff energy of plane-wave expansion was set to 400 eV. The Brillouin zone (BZ) was sampled using Monkhorst-Pack method with K points spacing less than 0.03*2π Å [28]. For density of states and charge density calculations, we doubled the number of K points for better accuracy. The energy convergence criterion was set to be 10^{-5} eV. Atomic positions were fully relaxed with the force acting on each atom being less than 0.01 eV/Å. Mirror layers are seperated with a vaccum layer of about 12 Å to avoid artificial interactions.

3. Results and discussion

3.1. Structure characterization

CFS//g@NC Janus heterostructures were obtained via the pyrolysis method involving a selenization of polydopamine (PDA)-coated Prussian blue analog. The PBA-derived carbon with high degree of graphitization uniformly wrapped Janus nanoparticles. As depicted in Fig. 1, the fabrication process of CFS//g@NC primarily consists of several stages. Initially, a cobalt iron Prussian blue analog (Co/Fe-PBA) is synthesized via a facile co-precipitation method. Figs. S1–3 show the crystal structure and morphology of the precursor. The raw materials employed in this process include $K_3[Fe(CN)_6]$ ($[Fe(CN)_6]^{3-}$), $CoCl_2{\cdot}6H_2O$ (Co^{2+}), and $C_6H_5O_7K_3{\cdot}2H_2O$ (a chelating agent). Due to the exceedingly small solubility product constant (Ksp) of PBA, immediate nucleation and grain growth occur once the raw material solutions are mixed. This poses a challenge in controlling the material's morphology, potentially leading to defects and agglomeration [29,30]. In order to address this issue, we introduced a chelating agent, $C_6H_5O_7K_3{\cdot}2H_2O$, capitalizing on its high chelating capacity with transition metal ions, thereby inhibiting the spontaneous nucleation and precipitation reaction of $Fe(CN)_6]^{3-}$. As a result, we are able to suppress spontaneous nucleus growth, facilitating the formation of a PBA with fewer defects and single-crystal growth. The primary reaction in the Co/Fe-PBA formation process can be represented as:

$$3Co^{2+} + 2[Fe(CN)_6]^{3-} \rightarrow Co_3[Fe(CN)_6]^2$$

Subsequently, dopamine is utilized for its catechol functional groups and terminal amino groups of lysine, providing superior adhesion. In alkaline environments, dopamine undergoes self-polymerization through an oxidative cross-linking reaction, forming a uniform, comprehensive layer of PDA. This PDA layer is coated onto the surface of Co/Fe-PBA. The resulting composite, Co/Fe-PBA@PDA, is then thermally decomposed to create a double-layered carbon structure (Co/Fe//g@NC), comprised of a graphite layer and an NC layer. This NC layer, transformed from a PDA film via high-temperature sintering, is a nitrogen-doped carbon layer that effectively moderates volume changes and prevent K_2Se from dissolving in the electrolyte [31].

Of note, the cyano group (C≡N) in Co/Fe-PBA forms a graphite layer during the thermal decomposition process. This in-situ formed graphite carbon layer, plays a role in hindering the CoFe alloy nanoparticles from aggregation. As a result, it helps in providing a greater number of active sites for catalysis. Following thermal decomposition, we selenize Co/Fe//g@NC, resulting in the formation of the CFS//g@NC. In this unique structure, each nanoparticle, including $CoSe_2$ and $FeSe_2$, is uniformly encapsulated by the graphite layer. This arrangement results in a heterostructure and double carbon layers, both of which enhance charge transfer and elevate the diffusion rate of potassium ions.

The crystal structure of the sample was confirmed by XRD measurements, as shown in Fig. 2a. The unique XRD pattern of the CFS//g@NC can be identified by the as the superposition of cubic $CoSe_2$ (Pa − 3 (205), JCPDS No. 04-003-1990) and orthorhombic $FeSe_2$ (Pnnm (58), JCPDS No. 04-003-1738), confirming the coexistence of $CoSe_2$ and $FeSe_2$ phases. No significant impurity peaks were observed in the XRD patterns. The diffraction peaks of $CoSe_2$//g@NC and $FeSe_2$//g@NC can be attributed to $CoSe_2$ and $FeSe_2$, respectively. As show in Fig. 2b, c and S4–6, the morphology and microstructure of the prepared CFS//g@NC, $CoSe_2$//g@NC, and $FeSe_2$//g@NC were characterized using field emission scanning electron microscopy (FESEM) and TEM. Fig. 2b and c show that small particle structures dispersed in the graphite and NC was observed through low − magnification TEM. The surface of the prepared

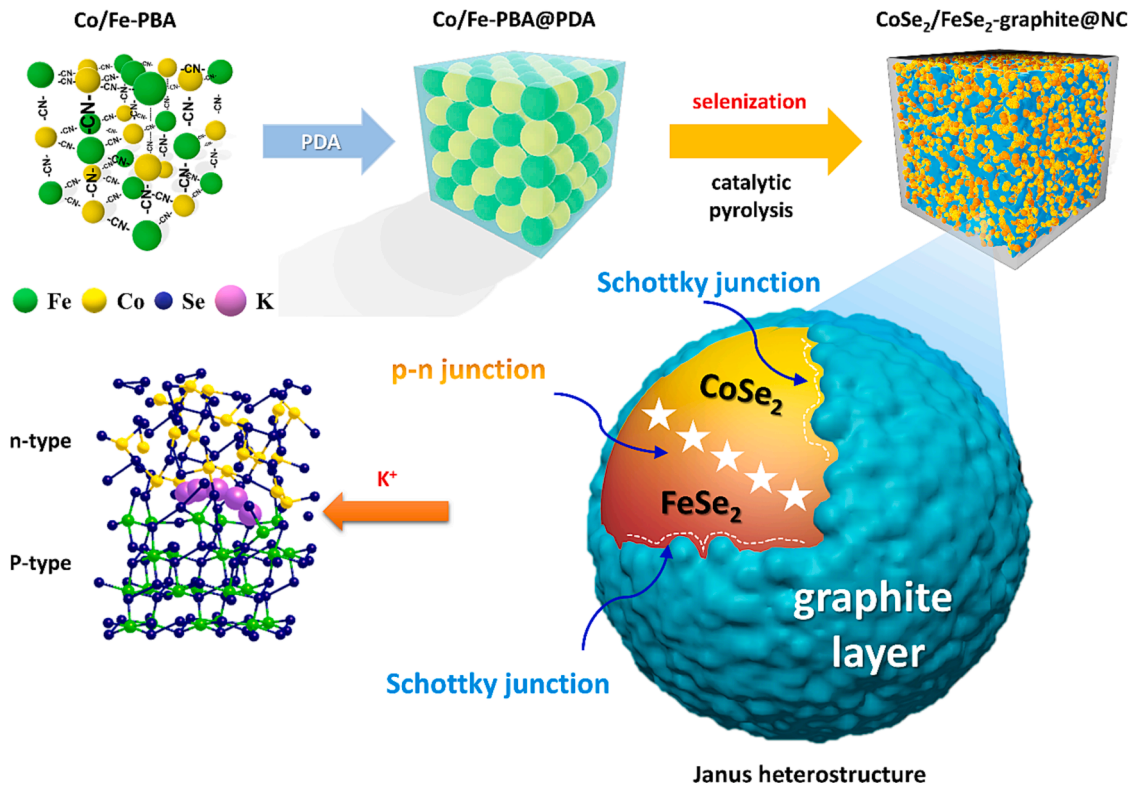

Fig. 1. Schematic diagram of the synthetic route of the CFS//g@NC Janus heterostructure.

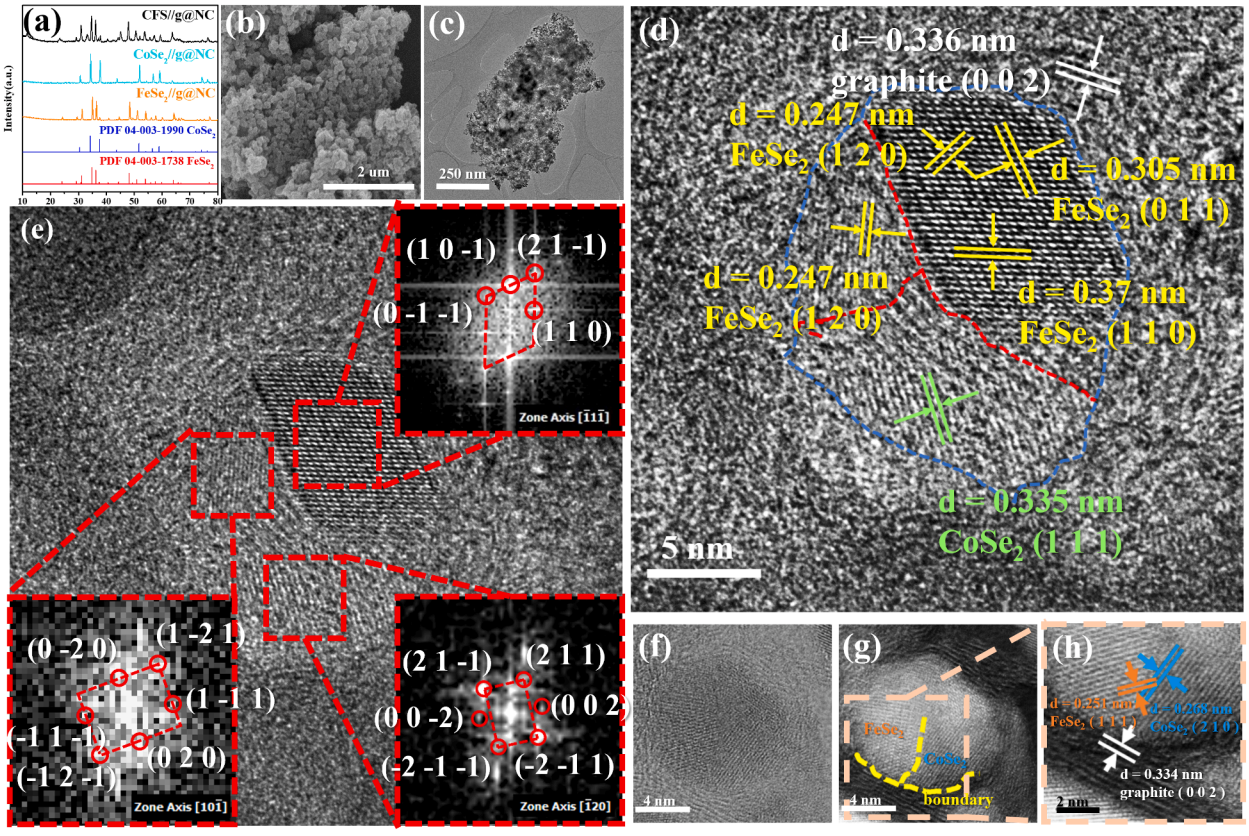

Fig. 2. (a) XRD pattern, (b) SEM image, (c) TEM image, (d) HRTEM image, (e) FFT, (f, g) HAADF-STEM images, and (h) HRTEM image of CFS//g@NC.

CFS//g@NC became noticeably rough and wrinkled after the carbonization and selenization [32]. In Fig. 2d, the high − resolution TEM (HRTEM) image of the CFS//g@NC shows lattice fringe spacings of 0.227, 0.247, and 0.37 nm in the upper region, corresponding to the (2 1 0), (1 2 0), and (1 1 0) planes of $FeSe_2$, respectively. The lower region shows a lattice fringe spacing of 0.335 nm, corresponding to the (1 1 1) plane of $CoSe_2$. On the other hand, the lattice spacing of 0.336 nm can be attributed to the (0 0 2) plane of the graphite layer generated by catalyzing the CN bond, confirming the successful formation of CFS//g@NC multilayer heterostructure [33–35]. The graphite layer with a thickness of 2–3 nm can promote electron transport. On the other hand, it was confirmed that a graphite layer wraps the CFS nanoparticle (Fig. S7). In addition, the corresponding fast Fourier transform (FFT) pattern confirms that CFS//g@NC is composed of $FeSe_2$ and $CoSe_2$ (Fig. 2e). The upper region correspond to the $[\bar{1}1\bar{1}]$ and $[10\bar{1}]$ zone axis of orthorhombic $FeSe_2$, respectively, the lower region corresponds to the $[\bar{1}20]$ zone axis of cubic $CoSe_2$ (Fig. S8) [22,36]. As depicted in Fig. 2f, the corresponding dark-field image allows for the clear identification of structural features (Fig. 2g and h). It also visibly shows the graphite layer wrapping around the $CoSe_2$ and $FeSe_2$ nanoparticles and presents a distinct boundary in the $CoSe_2/FeSe_2$ heterostructure. The lattice spacing d of 0.251 nm corresponds to the (1 1 1) plane of $FeSe_2$, the lattice spacing d of 0.268 nm corresponds to the (2 1 0) plane of $CoSe_2$, and the lattice spacing d of 0.334 nm corresponds to the (0 0 2) plane of graphite [37]. These results are also consistent with HRTEM and FFT.

We used dark-field imaging in TEM to confirm the presence of $CoSe_2$ and $FeSe_2$ in the Janus heterostructure. This method verified the structure of the CFS//g@NC, as shown in Fig. 3a and b. By tune position of the objective lens, the diffraction electron beam signal of a specific structure as the source of the main signal. The different signal results in the different bright area imaged in the dark field image, so as to infer the structure of CFS//g@NC. As shown in Fig. 3c and d, the signal of CFS//g@NC can be divided into two diffracted electron beam signals, $FeSe_2$ and $CoSe_2$. The diffracted beam is used for imaging, further the correspond dark field images of $FeSe_2$ and $CoSe_2$ were obtained. First, the diffraction rings in SAED correspond to the (2 1 1) and (2 3 0) planes of $FeSe_2$, the (2 2 0) plane of $CoSe_2$, and the (1 1 0) and (1 1 4) planes of graphite, indicating the coexistence of multiple phases in CFS//g@NC. The SAED of $CoSe_2$//g@NC and $FeSe_2$//g@NC are shown in Fig. S5b and S8b, respectively. In Fig. 3e and f, the bright areas can be seen to be the diffraction ring lattice signals contributed by the (2 2 0) plane of $CoSe_2$ and the (2 1 1) plane of $FeSe_2$, indicating that each particle in CFS//g@NC is composed of $FeSe_2$ and $CoSe_2$, further verifying the heterogeneous structure of CFS//g@NC. The dark-field image can be used to estimate the ratio of $CoSe_2$ and $FeSe_2$ in CFS//g@NC by counting the number of bright spots. In Fig. 3e, the number of bright spots lit by the diffraction electron beam provided by the (2 2 0) plane of $CoSe_2$ is calculated to be approximately 150. In Fig. 3f, the number of bright spots lit by the diffraction electron beam provided by the (2 1 1) plane of $FeSe_2$ is calculated to be approximately 170. The results show that the CFS//g@NC is composed of $CoSe_2$ and $FeSe_2$, the composition ratio is nearly 1:1. The results of Co/Fe-PBA are similar to this result (Figs. S9 and S10). Next, energy dispersive X-ray spectrometry (EDS) was used to analyze the composition and distribution of various elements. Fig. 3g shows that Co, Fe, Se, C, and N are uniformly distributed, further confirming the coexistence of $CoSe_2$ and $FeSe_2$ in the CFS//g@NC. The atomic percentage of Co: Fe: Se elements is approximately 23.3%: 14.1%: 62.7% (Figs. S11 and S12). The inductively coupled plasma-optical emission spectroscopy (ICP-OES) was performed. Table S1 shows that the weight percentage of Co: Fe: Se elements is 12.35 wt%: 7.06 wt%: 61.12 wt%. It can be determined that the atomic percentages of Fe:Co:Se elements are approximatey 11.1%: 18.9%: 70%, indicating the $CoSe_2$: $FeSe_2$ ratios of 1.7:1. In addition, the N element mapping completely overlaps with the carbon framework, indicating that NC is successfully dispersed in the CFS//g@NC.

XPS measurements were used to verify the valence band offsets of Fe

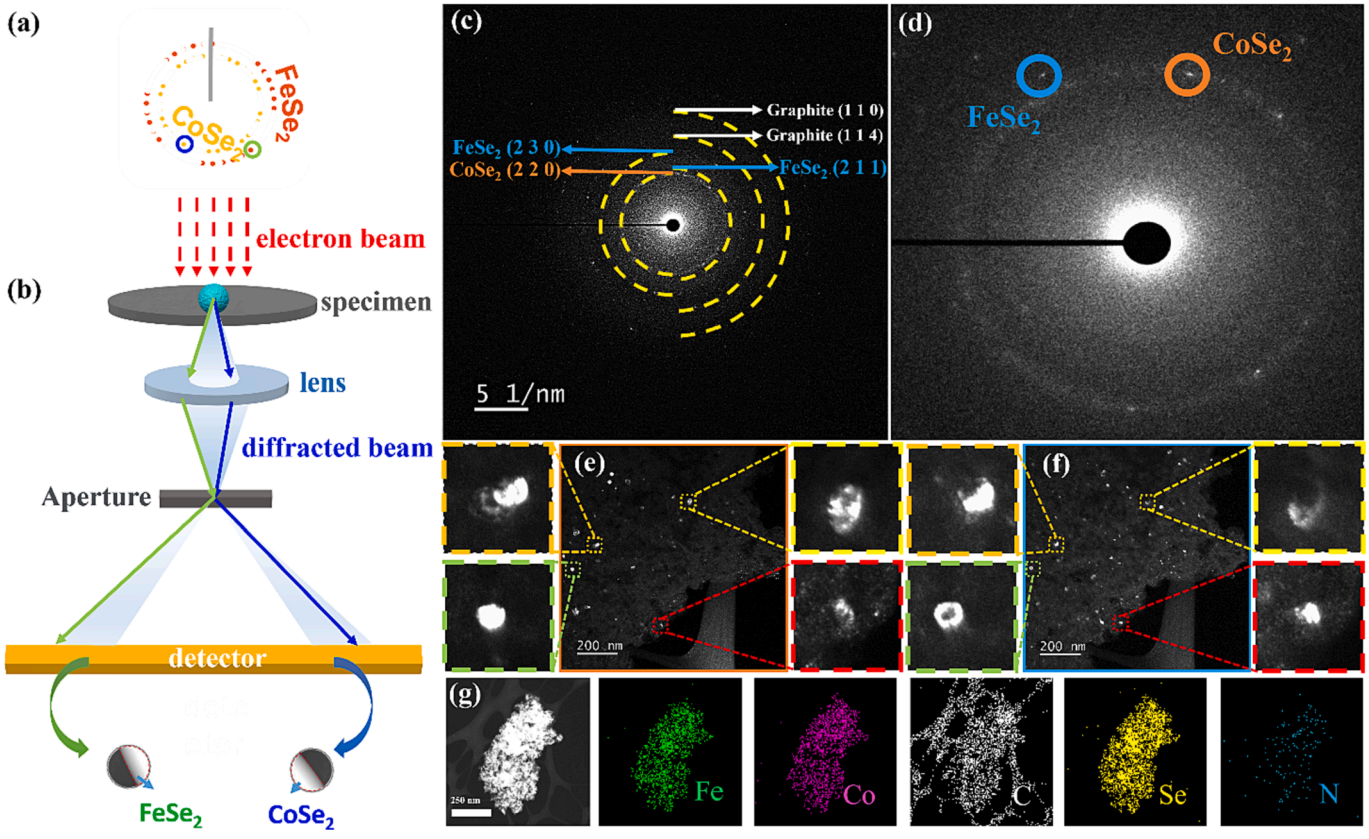

Fig. 3. (a, b) Schematic diagram of dark-field imaging. (c, d) SAED pattern, (e, f) dark-field image, and (g) EDS elements mapping of CFS//g@NC.

and Co species (Figs. S13 and S14). Driven by the built-in electric field from the heterojunction, it can be observed that the main peak in Fe $2p_{3/2}$ is significantly shifted to a lower binding energy (about 1 eV), confirming the strong electron interaction between $CoSe_2$ and $FeSe_2$. The Fe $2p_{3/2}$ of CFS//g exhibits a lower binding energy than that of $FeSe_2$//g. In contrast, the binding energy of Co $2p_{3/2}$ in CFS//g is higher than that of $CoSe_2$//g (about 1.4 eV), confirming the presence of some electron-deficient p-type $FeSe_2$ in CFS//g. The C 1 s further confirm formation of graphite carbon layers in the material [38–40]. Fig. S15 shows the Raman spectra of CFS//g with and without NC. The D band represents defects and disorder in the carbon material, while the G band represents the characteristic peak for the graphite. It can be confirmed that the graphite layer around $FeSe_2/CoSe_2$ is formed due to the catalytic generation of C≡N bonds. Similar results can be seen in the comparison materials (Fig. S16), verifying that cobalt and iron metals can catalyze the formation of graphite layer structures by C≡N bonds at high temperatures. The CFS//g@NC shows the BET specific surface area of 9.8351 $m^2 \cdot g^{-1}$ (Fig. S17). According to the TGA result in Figs. S18 and S19, the graphite and NC content for CFS//g could be calculated as 19.9% [41].

The bandgap (Eg) of the semiconductor can be estimated by the Tauc equation, using the ultraviolet–visible (UV–vis) spectrum. Notably, the absorption spectrum of indirect bandgap materials is steeper than that of direct bandgap materials. According to the Tauc plot (Fig. 4a), the bandgaps of $FeSe_2$//g and $CoSe_2$//g are calculated to be 1.50 eV and 1.18 eV, respectively. To further categorize the semiconductor type, UPS was performed on $FeSe_2$//g and $CoSe_2$//g (Fig. 4b). The valence band maximum (VBM) edges of $FeSe_2$//g and $CoSe_2$//g are 1.14 eV and 1.24 eV, respectively. The differential positioning of the Fermi level initiates spontaneous electron transfer, thus forming the built-in electric field at the heterostructure. The energy band diagram is displayed in Fig. 4c [42]. Connecting the n-type $CoSe_2$//g and p-type $FeSe_2$//g triggers electron flow from the filled states in the conduction band of $CoSe_2$//g to the vacant states in the valence band of $FeSe_2$//g until the Fermi levels of the two semiconductors equalize. The identical Fermi level prompts the energy bands of $CoSe_2$//g and $FeSe_2$//g to bend. The depletion region in $CoSe_2$//g and $FeSe_2$//g holds positive and negative charges, respectively [43]. The built-in electric field is formed upon contacting the p-type $FeSe_2$//g with n-type $CoSe_2$//g, which expedites the direct migration of electrons and potassium ions and optimizes the spatial distribution of charged species. In addition, the work function of $FeSe_2$, $CoSe_2$, $FeSe_2$//g, and $CoSe_2$//g was calculated using the formula: $\Phi = h\nu - E_{cutoff}$, where Φ is the work function, $h\nu = 21.22$ eV, and E_{cutoff} represents the cutoff energy. The E_{cutoff} of $FeSe_2$, $FeSe_2$//g, $CoSe_2$, and $CoSe_2$//g is 16.53, 17.08, 17.35, and 17.2 eV, respectively, resulting in calculated work functions of 4.67, 4.12, 3.85, and 4 eV, respectively. The direct

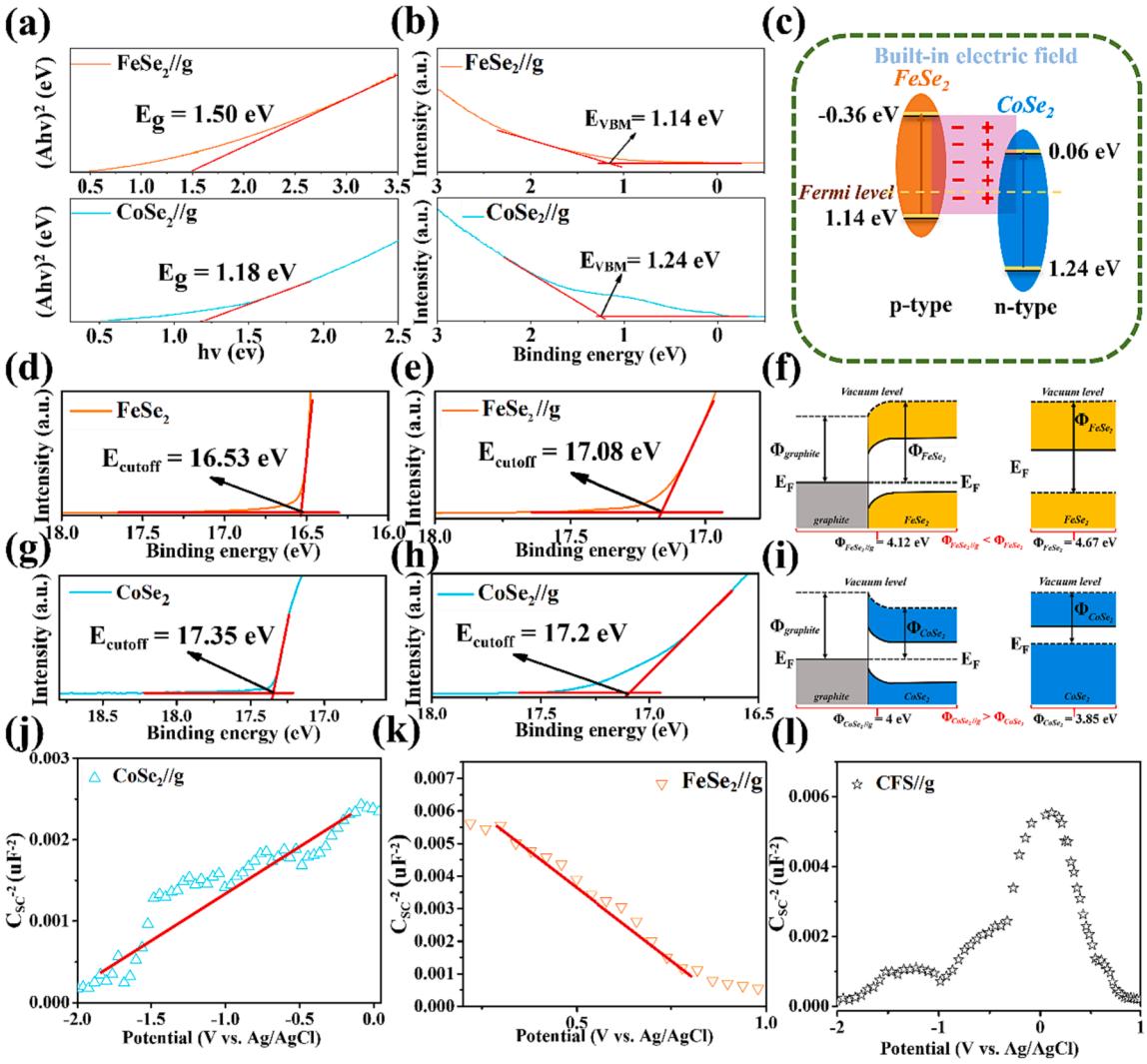

Fig. 4. (a) Tauc's bandgap plots, (b) UPS valence band spectra of $CoSe_2$//g and $FeSe_2$//g. (c) Band diagram for p-type $FeSe_2$ and n-type $CoSe_2$. (d, e) UPS spectra for the secondary electron cutoff region and (f) energy diagram of $FeSe_2$ and $FeSe_2$//g. (g, h) UPS spectra for the secondary electron cutoff region and (i) energy diagram of $CoSe_2$ and $CoSe_2$//g. The Mott-Schottky plots of (j) $CoSe_2$//g (k) $FeSe_2$//g and (l) CFS//g.

contact between a conductor and a semiconductor creates a Schottky barrier at the interface, causing adjustment between the materials. Rectification, leading to the formation of a Schottky junction, will occur if the work function of the n-type semiconductor is smaller than that of the conductor. Conversely, an opposing trend is observed when the material is a p-type semiconductor. Fig. 4d–f compare the work function values of $FeSe_2$ with and without a graphite layer, with the work function value of $FeSe_2$//g being smaller than that of p-type $FeSe_2$. When p-type $FeSe_2$ directly contacts the graphite layer, electrons spontaneously migrate from the graphite layer to $FeSe_2$ until the Fermi levels align. This self-driven charge density redistribution at the heterointerface is consistent with the Mott-Schottky heterojunction structure in solid-state physics. Conversely, the work function value of $CoSe_2$//g is larger than that of n-type $CoSe_2$ (Fig. 4g–i) [44]. The Fermi level gap between n-type $CoSe_2$ and the graphite layer triggers electron injection into the graphite layers from $CoSe_2$ until equilibrium is achieved. In equilibrium, the electron bands of $CoSe_2$ bend upward at the interface, and the electric field from $CoSe_2$ to the graphite layer persists, forming a Schottky heterojunction structure. Thus, it is inferred that CFS//g also displays a Schottky heterojunction structure between $CoSe_2$/$FeSe_2$ and the surrounding graphite layers [23,45]. Further, Mott-Schottky analysis was conducted to verify the semiconductor types of $FeSe_2$//g and $CoSe_2$//g. Fig. 4j shows a positive Mott-Schottky slope, indicating that $CoSe_2$//g is an n-type semiconductor [46]. Conversely, the Mott-Schottky plot of $FeSe_2$//g in Fig. 4k has a negative slope, suggesting it is a p-type semiconductor [47]. With a p-n heterojunction structure, the curve's inverted V shape, as shown in Fig. 4l, serves as evidence of the successful formation of the p-n junction in CFS//g, a conclusion that is confirmed by the results presented in Fig. 4c. As mentioned earlier, an internal electric field forms at the contact interface, facilitating the transfer of negatively charged electrons from n-type $CoSe_2$ to p-type $FeSe_2$, which in turn accelerates swift charge transfer and increases the diffusion rate of potassium ions [48].

The electronic and local structure of the CFS//g, $FeSe_2$//g and $CoSe_2$//g was further investigated using X-ray absorption fine structure (XAFS). The Co K-edge X-ray absorption near-edge structure (XANES) spectrums in Fig. 5a and b show that the adsorption edge of CFS//g shifts to the higher energy region relative to $CoSe_2$//g, indicating the high valence state of Co in CFS//g. In Fig. 5c, the coordination environment of Co atoms in Co-Se is identified by the extended X-ray absorption fine structure (EXAFS) spectroscopy. Due to the defects and synergistic effects formed by the heterostructure interface, the Co-Se peak intensity of CFS//g significantly increases compared to $CoSe_2$//g, indicating that the Co species has a higher coordination number in CFS//g [49,50]. Similarly, the Fe K-edge XANES spectrums show that the adsorption edge of CFS//g is slightly shifted to lower energy compared to $FeSe_2$//g (Fig. 5d and e), representing a higher reduction of Fe species in CFS//g state. Fig. 5f shows the intensity of Fe-Se peak in CFS//g is lower than that of $FeSe_2$//g due to the change of coordination environment and induced vacancies, showing the opposite trend to the Co-Se peak [51]. The results represent that electrons flow from the filled state in the n-type $CoSe_2$ conduction band to the empty state in the p-type $FeSe_2$ valence band due to the generation of the built-in electric field at the heterointerface and the driving force for electrons, further redistributing the interface charges. Wavelet transform (WT) analysis is used to further visually observe the Co-Se bond and Fe-Se bond of CFS//

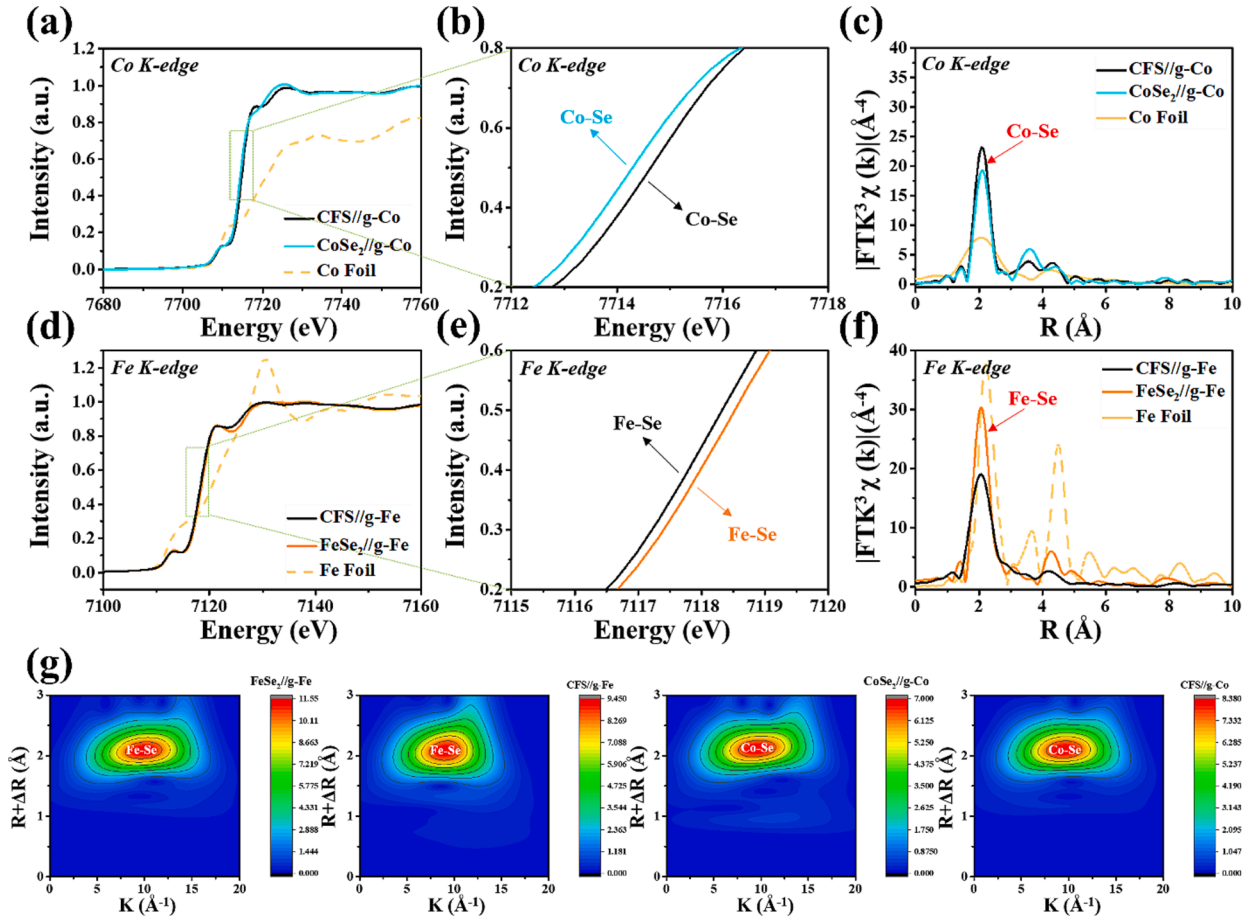

Fig. 5. (a, b) XANES spectra of Co K-edge, (c) EXAFS spectra of Co K-edge with Co Foil、$CoSe_2$//g and CFS//g. (d, e) XANES spectra of Fe K-edge, (f) EXAFS spectra of Fe K-edge with Fe Foil、$FeSe_2$//g and CFS//g. (g) Wavelet transforms for the k2-weighted Fe K-edge EXAFS signals for $FeSe_2$//g and CFS//g and Co K-edge EXAFS signals for $CoSe_2$//g and CFS//g.

g (Fig. 5g). And, due to the effect of the heterostructure interface, the Co-Se and Fe-Se bonds of CFS//g presents similar intensity (Co-Se: 8.38; Fe-Se: 9.45), which is different from $CoSe_2$//g (Co-Se: 7) and $FeSe_2$//g (Fe-Se: 11.55). The results show that Co-Se and Fe-Se bonds coexist in the CFS//g [37,52].

3.2. Electrochemical tests and analysis

The CV curves of the CFS//g@NC anode at a scan rate of 0.1 mV s^{-1} within the potential range of 0.001–3.0 V (vs. K^+/K) were demonstrated in Fig. 6a. An initial sharp reduction peak is observed during the cathodic scan, attributed to the formation of a solid electrolyte interface (SEI) layer via electrolyte decomposition. The CV curves for the first ten cycles exhibit similarity with those of $CoSe_2$//g@NC and $FeSe_2$//g@NC (Fig. S20), suggesting that the reduction reaction of CFS//g@NC could be similar to those of $CoSe_2$//g@NC and $FeSe_2$//g@NC [39,53]. This proposition is further supported by the examination of the potassium-ion storage mechanism in the CFS//g@NC electrode using ex-situ XPS and TEM measurements during the discharging/charging process. As shown in Fig. S21a, two peaks at 711.2 and 723.6 eV are related to $FeSe_2$ in the initial state. After discharging to 0.01 V, the peaks almost disappear because of the formation of Fe^0. On the contrary, the peaks at 711.2 and 723.6 eV appear at 3 V, demonstrating the reversible reaction. The Co spectrum also shows similar results (Fig. S21b). Fig. S21b shows the new peak appears after discharging to 0.01 V, which can be attributed to the formation of K_2Se. When charging to 3.0 V, the peak at 54.5 eV disappears, indicating the reversible conversion of K_2Se to $FeSe_2$/$CoSe_2$. In addition, the reversible reaction of CFS//g@NC can also be observed by ex situ TEM. The findings verify that the reaction mechanism of CFS//g@NC is similar to that of typical metal selenides [37].

The electrochemical performance of CFS//g@NC, assessed via coin-type half-cells assembly, displays the initial charge/discharge capacities of CFS//g@NC are 436.3 and 621.6 mA h g^{-1}, with an initial Coulombic efficiency (CE) of 70.2% at a current density of 50 mA g^{-1} (Fig. 6b). The low initial CE can be attributed to irreversible side reactions, such as electrolyte decomposition and SEI film formation [13]. After 50 cycles, CFS//g@NC shows a superior capacity to $CoSe_2$//g@NC and $FeSe_2$//g@NC, delivering 462.7 mA h g^{-1}. The specific capacity directly reflects the utilization efficiency of the conversion product (K_2Se), while the retention reflects the ability to suppress the shuttle effect. Notably, there is a gradual increase in capacity after an initial drop, leading to stability in subsequent cycles. This behavior is commonly seen in other reported transition metal chalcogenides and might be due to the formation of an organic polymer/gel-like layer during electrolyte decomposition, offering additional capacity via pseudocapacitive behavior. Furthermore, in order to explore the effect of the carbon layer on electrochemical performance, the cycling performance of the graphite and graphite coated with NC (graphite @NC) were investigated (Fig. S22). The result shows that NC doesn't contribute to the capacity, and the graphite layer doesn't contribute much to the capacity for the CFS//g@NC electrode. The galvanostatic charge − discharge (GCD) curves of the 1st and 50th cycles are shown in Fig. 6c and d. During the discharge process (blue frame), the first and the second plateau corresponds to the formation of the SEI layer and the conversion reaction, respectively. The overpotential of $CoSe_2$//g@NC is lower than $FeSe_2$//g@NC and CFS//g@NC due to a lower charge transfer resistance (Rct) during the solid–liquid phase transition process. When the charging voltage reaches 1.8 V (green frame), all materials undergo conversion reactions, but CFS//g@NC exhibits lower polarization and a longer plateau owing to higher utilization of K_2Se. With the inherent electric field provided by the p-n junction, the electrochemical performance of CFS//g@NC significantly outperforms other materials during the charge/discharge process [22,54]. On the contrary, $FeSe_2$//g@NC and $CoSe_2$//g@NC show a capacity decay after 50 cycles, contrasting with CFS//g@NC. This comparison confirms the efficacy of the p-n heterostructure design for enhanced potassium storage performance. Lastly, the layered structure of graphite benefits to volume change mitigation within the material, implying the crucial role of the Schottky junction in maintaining the anode's cycle stability. This conclusion is supported by consistent discharge and charge plateaus observable over 50 cycles for all three materials.

We examined the charge/discharge rates for different materials from 0.1 to 10 A g^{-1} to study the influence of p-n junctions and Schottky junctions on conversion kinetics (Fig. 6e and d). At the current density of 0.1, 0.2, 0.5, 1, 2, 4, 8, and 10 A g^{-1}, the reversible capacity of CFS//g@NC is 375, 351, 324, 310, 295, 271, 228, and 197 mA h g^{-1}, respectively. When the current density returns to 0.2 A g^{-1}, the capacity can recover to 368 mA h g^{-1}. When compared to $FeSe_2$@NC and $CoSe_2$@NC, the capacities of $FeSe_2$//g@NC and $CoSe_2$//g@NC remain stable at high rates. Defects between the graphite layers and $FeSe_2$/$CoSe_2$ enhance K^+ insertion/extraction during cycling, thereby improving their rate performance. Moreover, the abundant defects created at the interfaces increase the number of active sites, providing continuous diffusion paths for ions and electrons. Cycling performance is another indicator to evaluate the electrochemical stability and reversibility of the electrode. Fig. 6g shows the long-term cycling performance of the samples at a current density of 0.5 A g^{-1}. Remarkably, CFS//g@NC maintains a high reversible capacity of 195.4 mA h g^{-1} with a CE of 99.8% after 2500 cycles, surpassing $FeSe_2$//g@NC. This superior performance is attributed to the heterojunction and graphite-layered structure, which significantly enhance the material's performance and structural durability. As shown in Fig. 6h, the SEM image of CFS//g@NC's electrode surface shows no sign of cracks after 100 cycles. However, the electrode of the $FeSe_2$//g@NC and $CoSe_2$//g@NC cracks more severely than CFS//g@NC after 150 cycles (Fig. S23). The results can correspond to the result of Fig. 6g. The capacity of $FeSe_2$//g@NC and $CoSe_2$//g@NC decay quakily after 120 cycles. This suggests that CFS//g@NC nanoparticles can maintain their structure and good morphology during cycling, likely attributed to the buffering role of the graphite layer and NC layer [31].

The electrochemical kinetics of the electrodes were further investigated by measuring the electrochemical impedance spectra (EIS) of CFS//g@NC, $FeSe_2$//g@NC, and $CoSe_2$//g@NC after 100 cycles, respectively (Fig. 6i). The Nyquist plot, consisting of a depressed semicircle and a subsequent diffusion drift, reveals the charge transfer resistance (Rct) at the electrode/electrolyte interface. After 100 cycles, the Nyquist plot showed that the Rct of CFS//g@NC was smaller than that of $FeSe_2$//g@NC and $CoSe_2$//g@NC. Because Lower Rct value represents faster charge transfer behavior, it can be speculated that the p–n junction is beneficial to enhanced the charge transfer behavior of the material, further improving electrochemical performance. The relationship between the real part of EIS (Re(Z)) and the angular frequency ($\omega^{-0.5}$), in the low-frequency region of the three electrodes after 100 cycles is depicted in Fig. 6j. Calculated from the slope, the Warburg coefficients (σ) of CFS//g@NC, $FeSe_2$//g@NC, and $CoSe_2$//g@NC are 21.51, 29.11, and 37.96, respectively. CFS//g@NC, as indicated by its relatively lower gradient slope in the low-frequency region, allows a faster potassium ion diffusion rate compared to $FeSe_2$//g@NC and $CoSe_2$//g@NC. This increase in electrochemical kinetics contributes to the improved rate performance of CFS//g@NC, aligning with the results presented in Fig. 6e.

In comparison to $FeSe_2$//g@NC, CFS//g@NC merges the high capacity of $CoSe_2$//g@NC with the impressive cycling stability of $FeSe_2$//g@NC, creating a unique heterostructure material. This process not only reinforces the chemical bonds within the heterojunction, but also amplifies the built-in electric field, which in turn enhances the anode's structural stability. Consequently, the heterojunction interfaces exhibit improved charge transfer and accelerated potassium ion diffusion rates. Therefore, CFS//g@NC, featuring both p-n junctions and Schottky junctions, delivers superior rate performance and cycling stability. In terms of rate performance and long-term cycling, the CFS//g@NC anode outperforms other heterostructures or selenide/sulfide materials

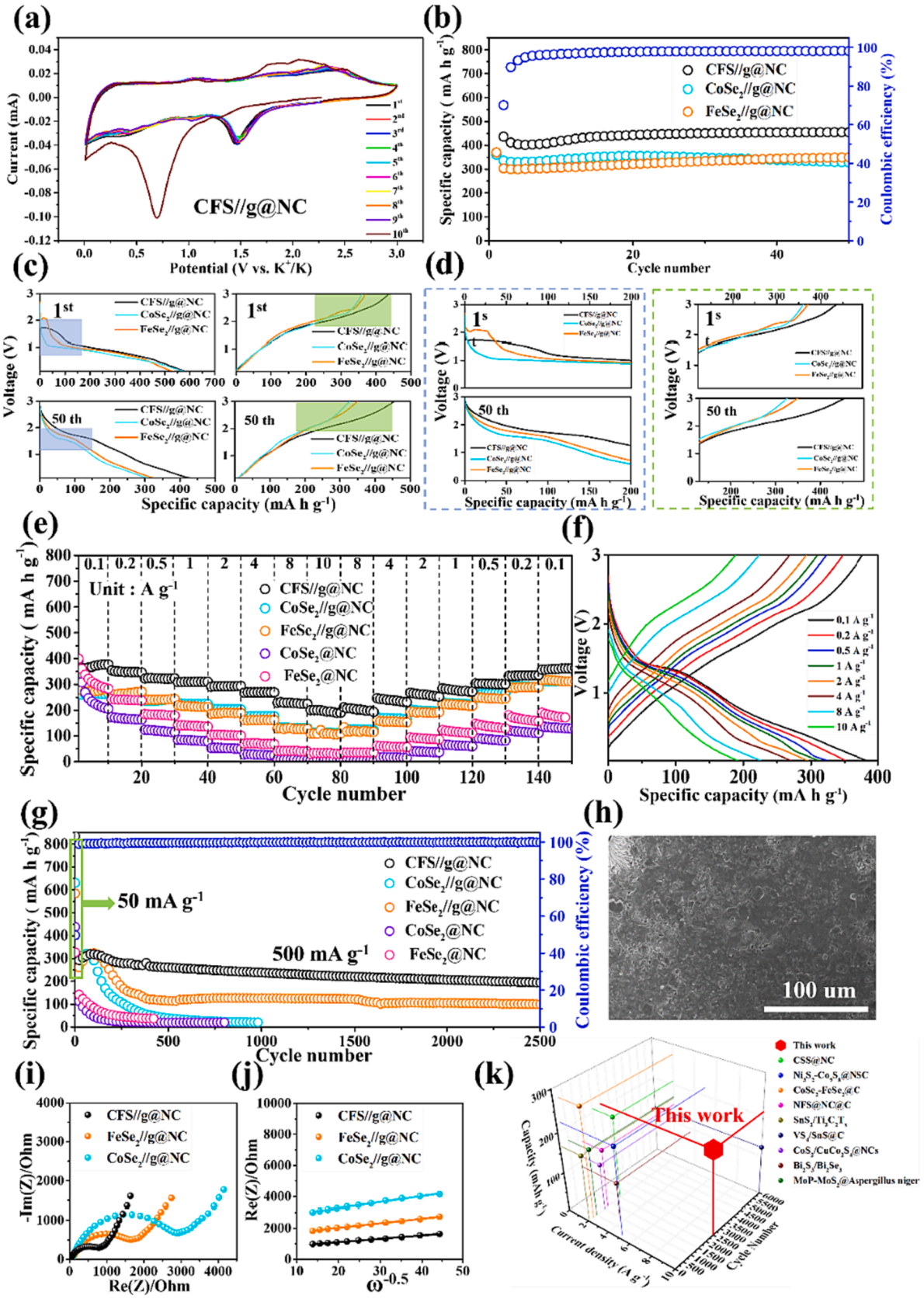

Fig. 6. (a) CV curves at 0.1 mV s^{-1}. (b) Cycling performance at 0.05 A/g. (c) GCD profiles with the 1st and 50th cycle at 0.05 A/g, (d) the corresponding plateau in discharge state (blue frame), and the corresponding plateau in charge state (green frame). (e) Rate capability and (f) the corresponding GCD profiles at various rates. (g) Long-term cycling performance at 500 mA g^{-1}. (h) SEM image of CFS//g@NC after 100 cycles. (i) Nyquist plots of CFS//g@NC, $FeSe_2$//g@NC and $CoSe_2$//g@NC after 100 cycles. (j) Linear diagram of impedance and frequency components in (i). (k) The comparison between this work and the other reported literatures. (For interpretation of the references to colour in this figure legend, the reader is referred to the web version of this article.)

(Fig. 6k) [22,37,55–61]. Notably, the rate and cycling performances of most materials, except for CFS//g@NC, are limited to around 5 A g^{-1} and fall below 2000 cycles. Although the capacity of most materials exceeds that of CFS//g@NC at lower rates, CFS//g@NC distinctly outshines them at high current densities (10 A g^{-1}) and over an extended number of cycles, demonstrating excellent rate capability and stable long-term cycling performance.

To explore the cause behind the superior rate capability of the CFS//g@NC heterostructure, CV measurements were conducted on 5 electrodes at various scan rates ranging from 0.1 to 0.9 mV s^{-1} (Fig. 7a and S24). Regardless of the scan rate, all CV curves present similar shapes, and as the scan rate increases, the cathodic and anodic peaks of the material can be seen gradually deviating from their original positions due to ohmic resistance. The kinetic behaviors of potassium-ion storage can be assessed using the following equation:

$$i = av^b \ (0.5 \leq b \leq 1) \quad (1)$$

$$\log i = \log a + b \log v \quad (2)$$

Eq. (1) illustrates the relationship between peak current (i) and scan rate (v), where a and b are adjustable constants. Based on the slope of the log(υ) vs. log(i) plot, b values of 0.5 or 1.0 correspond to diffusion-

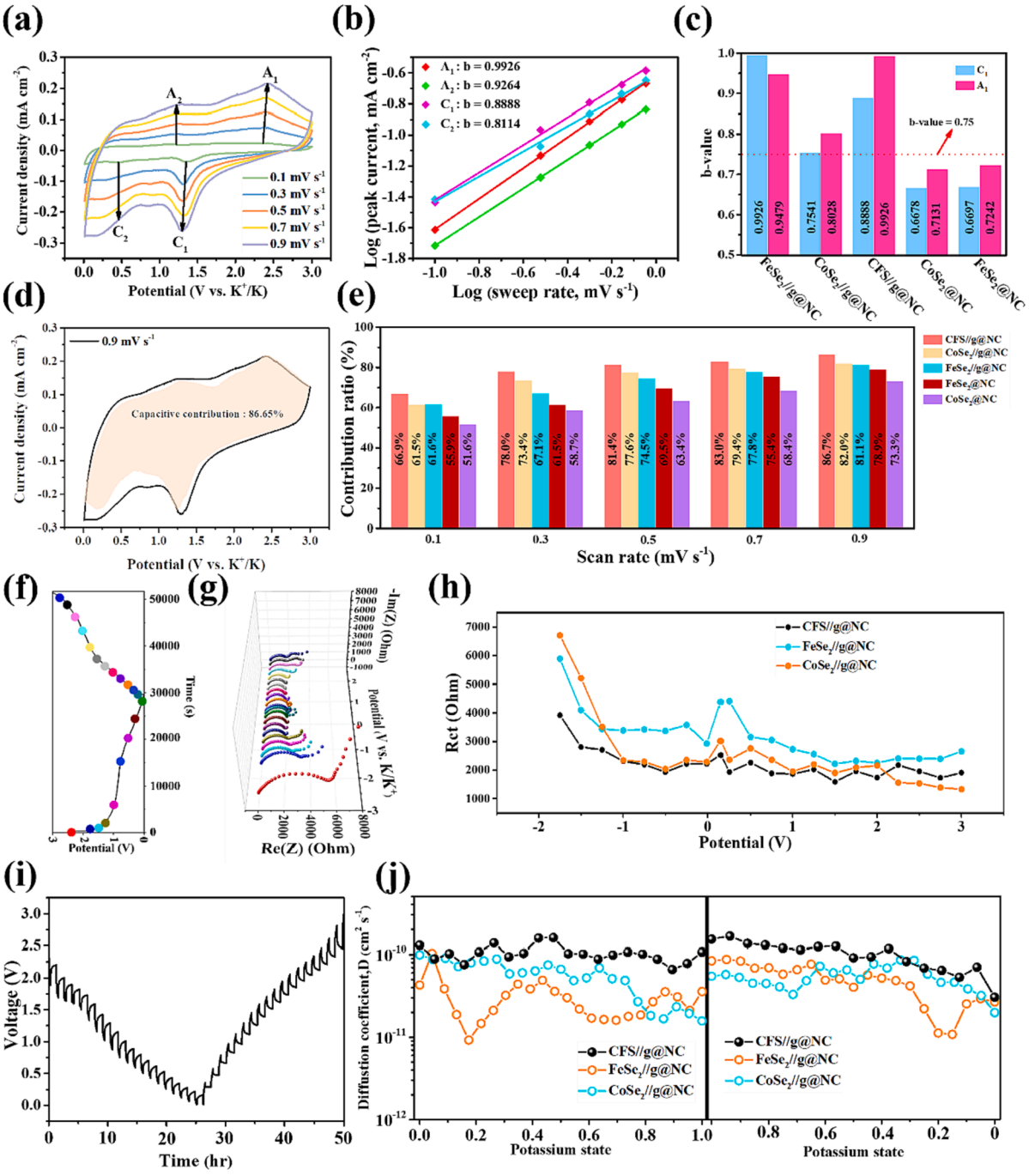

Fig. 7. (a) CV curves of CFS//g@NC at different scan rates. (b) The corresponding b values in linear regression. (c) Calculated b values for anodic and cathodic reactions. (d) The composition of pseudocapacitive characteristics in the CV curve at a scan rate of 0.9 mV s^{-1}. (e) Capacitive-controlled contribution at different scan rates. (f) Voltage profile, (g) Nyquist plot of CFS//g@NC, and (h) measured charge transfer resistance of all electrodes, derived from in-situ EIS analysis for the 1st cycle. (i) GITT curves with 20 mins current pulse of 50 mA g^{-1} followed by 60 mins relaxation and (j) corresponding diffusion coefficients of each current pulse.

controlled or capacitive-controlled electrochemical processes, respectively. The calculated b values for peaks A1, A2, C1, and C2 in CFS//g@NC are 0.9926, 0.9264, 0.8888, and 0.8114, respectively (Fig. 7b) [62]. The b values calculated for $CoSe_2$//g@NC and $FeSe_2$//g@NC are also similar to those of CFS//g@NC and exceed 0.75 (Fig. S25). Although $CoSe_2$@NC and $FeSe_2$@NC have similar CV curves to $CoSe_2$//g@NC and $FeSe_2$//g@NC, their calculated b values are less than 0.75. The nearly 1.0 'b' values for CFS//g@NC, $CoSe_2$//g@NC, and $FeSe_2$//g@NC suggest a pseudocapacitive-driven potassium-ion storage mechanism (Fig. 7c), indicating the critical role of p-n and Schottky junctions in enhancing the high rate performance. To quantify the contribution of the capacitive-controlled process, a specific relationship equation is employed to compute the constant k.

$$i = k_1v + k_2v^{0.5} \quad (3)$$

where k_1v represents non-Faradaic reactions, and $k_2v^{0.5}$ represents Faradaic reactions. The CV of CFS//g@NC at 0.9 mV s^{-1} is shown in Fig. 7d, and the percentage of capacitive contribution relative to the total area is 86.65%. Fig. S26 shows the CV of the other sample at 0.9 mV s^{-1}. The capacitive-controlled current on the inner surface exceeds the diffusion-controlled current, and as highlighted in Fig. 7e and S27, the surface capacitive effect of CFS//g@NC is more pronounced compared to the four anodes, summarizing all capacitive processes across different scan rates. The capacitive contribution increases with the scan rate, indicating the high rate potassium storage capability. These high capacitive contributions also indicate the fast charge/discharge characteristics of CFS//g@NC, $CoSe_2$//g@NC, and $FeSe_2$//g@NC electrodes. To further investigate the changes in Rct values during the first potassiation and depotassiation processes, *in-situ* EIS analysis was conducted (Fig. 7f – h; Fig. S28) [22,37,53]. Due to the heterogeneous structure of CFS//g@NC, the Rct values are initially lower in the potassiation process than those of $CoSe_2$//g@NC and $FeSe_2$//g@NC, and the Rct values of all the electrodes show a gradually decreasing trend in the potassiation process. Different from $FeSe_2$//g@NC, CFS//g@NC has no large fluctuations between 0 and 1 V because the p-n junction promotes the diffusion of potassium ions and the conversion reactions. For the depotassiation process, the p-n heterostructure makes CFS//g@NC structurally stable, and thus there is no significant difference in Rct values. $CoSe_2$//g@NC, being an electron-rich n-type semiconductor, exhibits lower Rct values, but its stability and cyclic performance are inferior. Due to the formation of p-n and the Schottky junction, CFS//g@NC exhibits the excellent capacitance performance and lower Rct values. To study the diffusion kinetics of CFS//g@NC, $CoSe_2$//g@NC, and $FeSe_2$//g@NC, GITT was used to measure the diffusion coefficient of K^+ (D_{K+}) in Fig. 7i. For the linear relationship between Eτ and $\tau^{1/2}$ shown in Fig. S29 [63], the D_{K+} values of CFS//g@NC, $CoSe_2$//g@NC, and $FeSe_2$//g@NC were calculated from the GITT curves according to the equation:

$$D_{K+} = \frac{4}{\pi\tau}L^2\left(\frac{\Delta Es}{\Delta Et}\right)^2 \quad (4)$$

where τ is the current pulse time (s); L is the electrode thickness, which are determined from the cross-sectional SEM images in Fig. S30; ΔEs is the constant voltage change induced by the current pulse; ΔEt is the potential change of the steady-state current pulse. As shown in Fig. 7j, the CFS//g@NC electrode (>-10^{-10} cm^2 s^{-1}) has a higher D_{K+} compared to $CoSe_2$//g@NC and $FeSe_2$//g@NC electrodes in the range of ≈10^{-11}–10^{-10} cm^2 s^{-1}, indicating that the heterointerface of the CFS//g@NC electrode promotes the diffusion of K^+ [64–66].

3.3. Energy band diagram, KPFM analysis and DFT calculations

The energy band diagram of $FeSe_2$, $CoSe_2$, and graphite layers after Fermi level equilibration is depicted in Fig. 8a. Through direct contact with the graphite layer and n-type semiconductor $CoSe_2$, the p-type $FeSe_2$ semiconductor acquires electrons, concentrating electrons in $FeSe_2$ and enhancing its ability to attract potassium ions. By means of p-n and Schottky heterojunction interactions, $FeSe_2$ accumulates more electrons compared to a typical p-type semiconductor, and $CoSe_2$ loses more electrons compared to a standard n-type semiconductor. This dynamic creates a robust built-in electric field between $FeSe_2$ and $CoSe_2$, drastically enhancing the diffusion rate of potassium ions and thereby augmenting the rate performance of CFS//g@NC. The KPFM technique, which determines surface potential differences by measuring surface charge density, has been established as an effective method to study built-in electric fields. The surface potential differences of CFS//g, $FeSe_2$//g, and $CoSe_2$//g were examined, as presented in Fig. 8b and c. CFS//g displays the highest surface potential (ΔE = 170.13 mV), while the surface potentials of $FeSe_2$//g and $CoSe_2$//g are 59.36 and 64.24 mV, respectively. These findings imply that the p-n heterojunction structure of CFS//g generates a built-in electric field, reducing internal resistance and fostering electron and ion interfacial transport. Hence, the negatively charged $FeSe_2$ can more effectively capture potassium ions, while electrons are propelled towards the positively charged $CoSe_2$, improving battery performance and substantially enhancing charge separation and transport. Moreover, surface potential measurements reveal that the potential of $CoSe_2$//g is lower than that of $FeSe_2$//g (Fig. 8d), indicating that under the impetus of the built-in electric field, the electrons of CFS//g move from the $CoSe_2$ side to the $FeSe_2$ side, instigating the redistribution of interfacial charges at the heterojunction interface [67–69]. In the EPR spectrum, signal broadening and amplification indicate the existence of defect sites in the material. Importantly, the signal intensity of CFS//g is significantly stronger than that of $FeSe_2$//g and $CoSe_2$//g. This shows that CFS//g, which contains both p-n and Schottky heterojunctions, exposes more defect sites as seen in Fig. 8e [70,71].

To study the influence of the constructed heterointerface on reaction kinetics, the DFT calculations were performed. The density of states (DOS) and partial density of states (PDOS) for $FeSe_2$, $CoSe_2$, and CFS are shown in Fig. 8f, S31 and S32, respectively. The bandgap of the $FeSe_2$ monolayer is quite narrow, with the conduction and valence band edges primarily composed of Fe – d states, accompanied by minor participation of Se – p states. In contrast, the $CoSe_2$ monolayer exhibits a metallic character, devoid of a bandgap. The hybridization of Se – p and Co – d states near the Fermi level indicates a high density of charge carriers, suggesting excellent electronic conductivity in the $CoSe_2$ monolayer. Notably, the bandgap of CFS near the Fermi level undergoes a shift, suggesting improved conductivity compared to the $FeSe_2$ and $CoSe_2$ monolayers [72,73]. The good electronic conductivity has higher utilization of active materials and promotes ion diffusion kinetics to improve the electrochemical properties of electrode materials [74]. Fig. 6 shows the electrochemical performances of CFS//g@NC are better than those of $FeSe_2$//g@NC and $CoSe_2$//g@NC. Fig. 8g visualizes the charge density, revealing the distribution of electrons in both depletion (green) and accumulation (yellow) regions, thus verifying the direction of electron contribution and transfer. In the $FeSe_2$/$CoSe_2$ interface, most of the charge is predominantly concentrated near the Co side, with the depleted portion surrounding the Fe and Se atoms. This observation is consistent with the discussion in Fig. 4c, which describes the electron flow from the n-type $CoSe_2$ to the p-type $FeSe_2$. Fig. 8h demonstrates that the charge and dissipative regions of CFS are concentrated near the Se and K atoms and the Co and Fe atoms, respectively. The charge transfers from $CoSe_2$ to $FeSe_2$, promoting electron transfer to form an electron transport pathway and further confirming the unbalanced charge distribution in the computational results [46]. Furthermore, we investigate the internal diffusion potential barrier of the CFS heterostructure (Fig. 8i, j and S33 – S35). As shown in Fig. 8i, the energy barrier of K atoms on the CFS heterostructure is 0.28, 0.45, 0.26, 0.35, and 0.15 eV. The diffusion barrier of K is slightly two times smaller on the CFS heterostructure (0.45 eV) than on $FeSe_2$ (0.90 eV) and $CoSe_2$ (0.89 eV). Owing to the formation of the heterointerface, CFS exhibits a

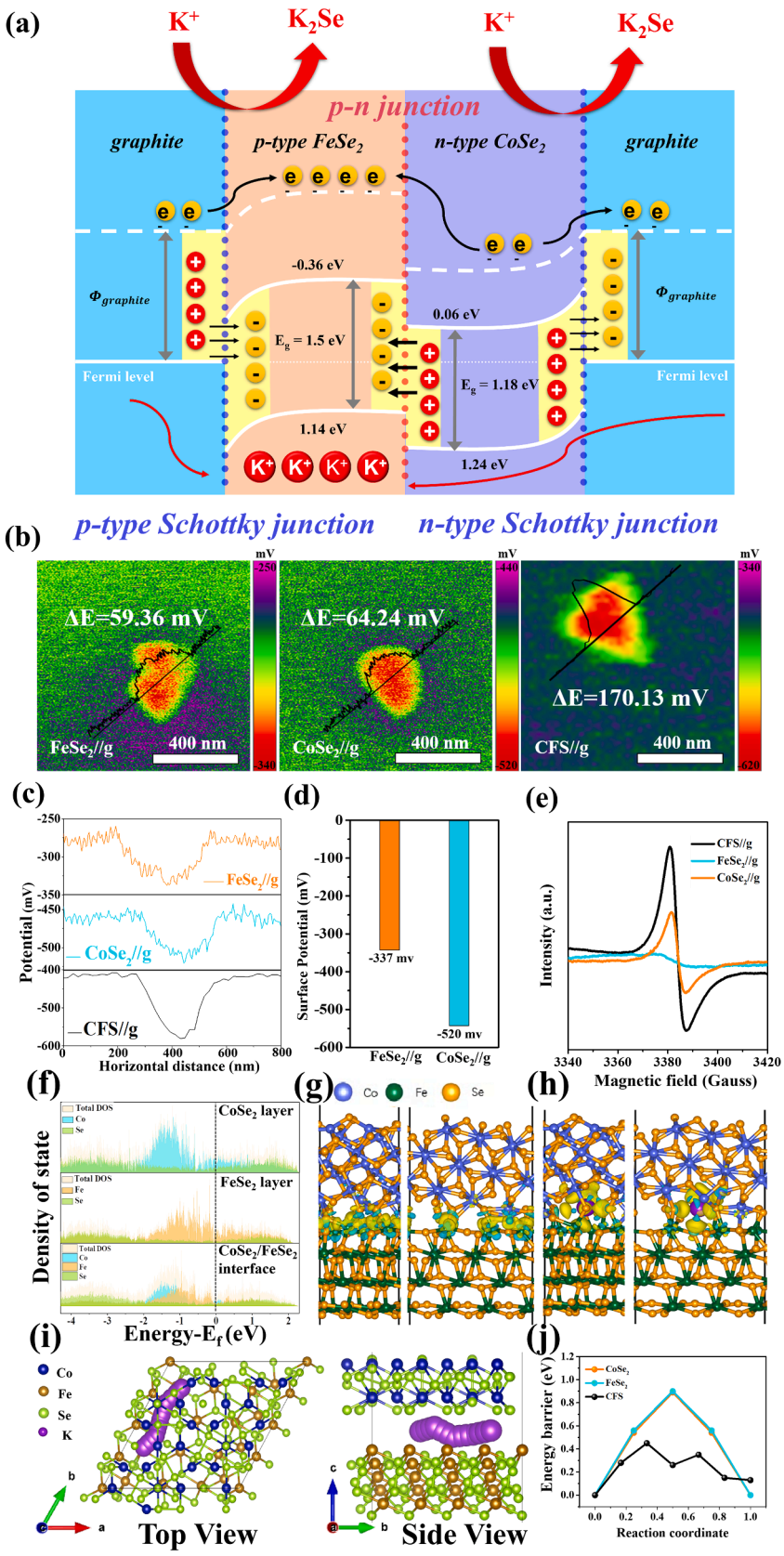

Fig. 8. (a) Energy diagram of CFS//g. (b) KPFM image of $FeSe_2$//g, $CoSe_2$//g and CFS//g and the corresponding (c) surface potential profiles. (d) Comparison of the surface potential of $FeSe_2$//g and $CoSe_2$//g. (e) EPR spectra of CFS//g, $FeSe_2$//g and $CoSe_2$//g. (f) DOS and PDOS of $CoSe_2$ monolayer, $FeSe_2$ monolayer, and CFS. (g, h) charge density difference of CFS before and after K^+ insertion. (i) Diffusion path in top view and side for heterostructure. (j) Comparison of energy barrier of K^+ diffusion.

lower diffusion energy barrier under the condition of built-in electric field generation. Therefore, the construction of the heterostructure not only significantly promotes the diffusion of K^+ intermediates but also greatly facilitates charge transfer and ion diffusion during cycling [75].

3.4. Discussion

Fig. 9 introduces strategies to boost the electrochemical performance of potassium ions within materials, utilizing heterostructure construction and PBA-derived carbon layers. It specifically depicts the characteristics of diverse materials like CFS//g@NC and MSe_2@NC (where M is either Co or Fe), and shows them both with and without an accompanying graphite layer. Numerous studies have employed diverse carbon coatings—like graphene, porous carbon, biomass carbon materials, and citric acid-derived carbon or NC—to enhance the performance of these materials [76–78]. Despite these efforts, MSe_2 materials wrapped in NC, specifically $FeSe_2$@NC and $CoSe_2$@NC, demonstrate poor cyclic performance (fewer than 200 cycles) under 500 mA g^{-1}. This underperformance is due to the intrinsic volumetric expansion and shuttle effect of MSe materials, which lead to substantial structural fracturing. A single NC layer appears inadequate to fully alleviate this issue. In response to this challenge, we introduced a PBA-derived graphite layer to MSe, forming a second protective layer. This layer creates a Mott-Schottky heterojunction with the MSe, leading to a higher concentration of electrons. Interestingly, the $FeSe_2$//g@NC shows a greater electron concentration, thus attracting more potassium ions compared to $CoSe_2$//g@NC. As a result, the electrochemical performance of $FeSe_2$//g@NC surpasses that of $CoSe_2$//g@NC, as demonstrated in Fig. 9b. To preserve the structural integrity of MSe, we implemented a dual-layer carbon structure. The PBA-derived graphite layer encapsulates the MSe, preventing nanoparticle agglomeration. This graphite layer also generates an intrinsic electric field that accelerates charge transfer and improves reaction kinetics during discharge/charge cycles. Nevertheless, in long cycle stability tests, the capacitance of $FeSe_2$//g@NC and $CoSe_2$//g@NC started to decline after 200 cycles. The introduction of a graphite layer did not result in a significant improvement in either capacitance or stability.

Furthermore, a dual heterostructure, CFS//g@NC, following the introduction of a p-n heterojunction is constructed. The p-type $FeSe_2$ semiconductor, through direct contact with the graphite layer and n-type semiconductor $CoSe_2$, acquires electrons, which then accumulate in $FeSe_2$ and enhance its ability to attract potassium ions. In contrast, the n-type $CoSe_2$ loses more electrons. The formation of the graphite layer augments the internal electric field between $FeSe_2$ and $CoSe_2$, significantly enhancing potassium ion diffusion and improving the rate performance of CFS//g@NC. As shown in Fig. 9c, the combination of the dual heterojunction and the graphite layer in CFS//g@NC results in improved cycle stability and rate performance. The p-n junction interface between $CoSe_2$ and $FeSe_2$ facilitates the diffusion path for potassium ion insertion, thereby significantly boosting potassium ion storage kinetics and potassium atom dispersion. The Schottky heterojunction aids the function of the p-n junction, while the graphite layer buffers the expansion of the active materials, thereby maintaining robust structural integrity and excellent reaction kinetics. Consequently, CFS//g@NC exhibits superior rate performance under 10 A g^{-1}, and maintains this high performance level for an extended cycle life of up to 2500 cycles.

4. Conclusions

In summary, the CFS//g@NC was prepared by a facile catalytic pyrolysis and selenization of PBA combined with PDA-derived carbon coating, and employed as anode electrode in PIB. By designing the Janus heterostructure configuration, the enriched heterointerface contact significantly enhances the reaction electrochemical kinetics of the conversion mechanism, which can be verified in experiments and simulations. Due to the synergistic effect of the dual heterojunction, potassium ions are more easily concentrated near the $FeSe_2$ side. This unique design not only changes the electronic structure but

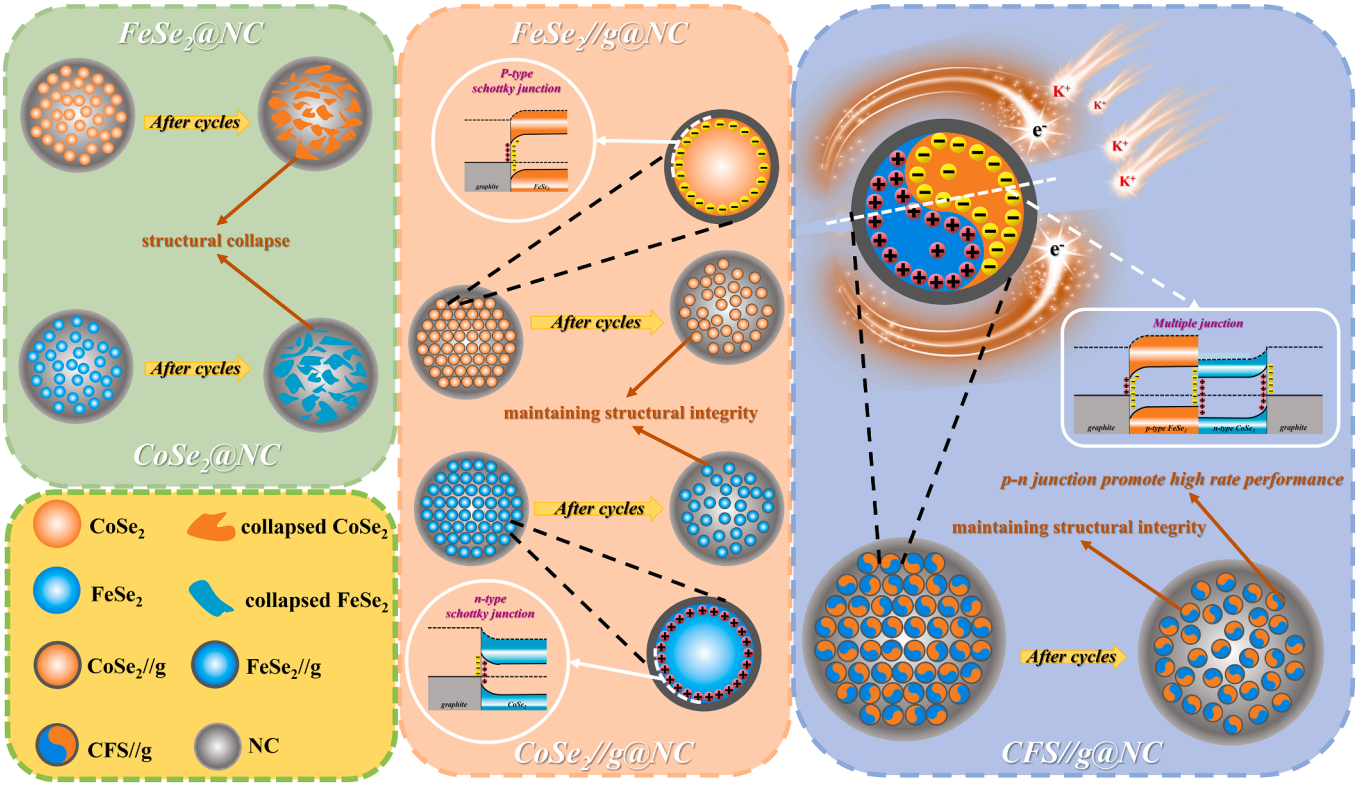

Fig. 9. Schematic illustration of the reaction process of (a) $FeSe_2$@NC and $CoSe_2$@NC, (b) $FeSe_2$//g @NC and $CoSe_2$//g@NC, (c) CFS//g@NC anodes for PIBs.

also enhances K^+ diffusion. These experimental results confirm the presence of both p-n junctions and Schottky junctions, providing a larger built − in electric field for the CFS//g@NC, enhancing its pseudocapacitive capability, lower Rct values, and higher potassium ion diffusion coefficient, which significantly improve the rate performance. In addition, designing electrode materials coupling with a graphite layer and NC provides robust shell protection to demonstrate excellent cycling durability. The CFS//g@NC exhibited excellent electrochemical performance benefiting from the p-n junctions, Schottky junctions and the protection of the carbon layer. As expected, the CFS//g@NC was endowed with superior rate capability and excellent cycling stability with more than 2500 cycles. Given the excellent rate performance generated by the interface contact structure and synergistic effect of the Janus heterostructure, this study provides a reliable approach for the rechargeable energy storage.

Declaration of Competing Interest

The authors declare that they have no known competing financial interests or personal relationships that could have appeared to influence the work reported in this paper.

Data availability

No data was used for the research described in the article.

Acknowledgements

This work received financial support from the 2030 Cross-Generation Young Scholars Program by National Science and Technology Council, Taiwan (NSTC 112-2628-E-007-010). H.-Y. Tuan also acknowledges the financial support of National Tsing Hua University, Taiwan, through Grant No. 112B0011J2.

Appendix A. Supplementary data

Supplementary data to this article can be found online at https://doi.org/10.1016/j.cej.2023.145992.

References

[1] C.-Y. Tsai, C.-H. Chang, T.-L. Kao, K.-T. Chen, H.-Y. Tuan, Shape matters: $SnP_{0.94}$ teardrop nanorods with boosted performance for potassium ion storage, Chem. Eng. J. 417 (2021), 128552.
[2] X. Min, J. Xiao, M. Fang, W.A. Wang, Y. Zhao, Y. Liu, A.M. Abdelkader, K. Xi, R. V. Kumar, Z. Huang, Potassium-ion batteries: outlook on present and future technologies, Energ. Environ. Sci. 14 (4) (2021) 2186–2243.
[3] W. Zhang, Y. Liu, Z. Guo, Approaching high-performance potassium-ion batteries via advanced design strategies and engineering, Sci. Adv. 5 (5) (2019) eaav7412.
[4] J. Zheng, C. Hu, L. Nie, H. Chen, S. Zang, M. Ma, Q. Lai, Recent Advances in Potassium-Ion Batteries: From Material Design to Electrolyte Engineering, Adv. Mater. Technol. (2023) 2201591.
[5] Q. Zhang, Z. Wang, S. Zhang, T. Zhou, J. Mao, Z. Guo, Cathode materials for potassium-ion batteries: current status and perspective, Energy Rev. 1 (2018) 625–658.
[6] J. Yang, Z. Ju, Y. Jiang, Z. Xing, B. Xi, J. Feng, S. Xiong, Enhanced capacity and rate capability of nitrogen/oxygen dual-doped hard carbon in capacitive potassium-ion storage, Adv. Mater. 30 (4) (2018) 1700104.
[7] Y. Xu, H. Zhang, T. Ding, R. Tian, D. Sun, M.-S. Wang, X. Zhou, Synthesis of yolk-shell Bi_2O_3@ TiO_2 submicrospheres with enhanced potassium storage, Sci. China Chem. 65 (9) (2022) 1807–1816.
[8] S. Liu, L. Kang, J. Henzie, J. Zhang, J. Ha, M.A. Amin, M.S.A. Hossain, S.C. Jun, Y. Yamauchi, Recent advances and perspectives of battery-type anode materials for potassium ion storage, ACS Nano 15 (12) (2021) 18931–18973.
[9] Y. Du, Z. Zhang, Y. Xu, J. Bao, X. Zhou, Metal sulfide-based potassium-ion battery anodes: storage mechanisms and synthesis strategies, Acta Phys.-Chim. Sin 38 (2022) 2205017.
[10] Z. Zhang, L. Duan, Y. Xu, C. Zhao, J. Bao, J. Shen, X. Zhou, Synthesis of multicore-shell FeS_2@ C nanocapsules for stable potassium-ion batteries, J. Energy Chem. 73 (2022) 126–132.
[11] A. Eftekhari, The rise of lithium–selenium batteries, Sustain. Energy Fuels 1 (1) (2017) 14–29.
[12] I. Hussain, S. Sahoo, C. Lamiel, T.T. Nguyen, M. Ahmed, C. Xi, S. Iqbal, A. Ali, N. Abbas, M.S. Javed, K. Zhang, Research progress and future aspects: Metal selenides as effective electrodes, Energy Storage Mater. 47 (2022) 13–43.
[13] C.A. Etogo, H. Huang, H. Hong, G. Liu, L. Zhang, Metal–organic-frameworks-engaged formation of $Co_{0.85}Se$@C nanoboxes embedded in carbon nanofibers film for enhanced potassium-ion storage, Energy Stor. Mater. 24 (2020) 167–176.
[14] Y. Liu, Q. Wan, J. Gong, Z. Liu, G. Tao, J. Zhao, L. Chen, W. Li, X. Wei, L. Ni, Confine, Defect, and Interface Manipulation of Fe3Se4/3D Graphene Targeting Fast and Stable Potassium-Ion Storage, Small 19 (8) (2023) 2206400.
[15] T. Li, Y. Wang, L. Yuan, Q. Zhou, S. Qiao, Z. Liu, S. Chong, An α-MnSe nanorod as anode for superior potassium-ion storage via synergistic effects of physical encapsulation and chemical bonding, Chem. Eng. J. 446 (2022), 137152.
[16] M. Lee, T.W. Kim, C.Y. Park, K. Lee, T. Taniguchi, K. Watanabe, M.-G. Kim, D. K. Hwang, Y.T. Lee, Graphene Bridge Heterostructure Devices for Negative Differential Transconductance Circuit Applications, Nanomicro Lett. 15 (1) (2023) 1–11.
[17] A. Zhong, Y. Zhou, H. Jin, H. Yu, Y. Wang, J. Luo, L. Huang, Z. Sun, D. Zhang, P. Fan, Superior Performances of Self-Driven Near-Infrared Photodetectors Based on the SnTe: Si/Si Heterostructure Boosted by Bulk Photovoltaic Effect, Small 19 (14) (2023).
[18] M. Zhang, Y. Lin, J. Li, X. Wei, Y. Peng, Z. Wang, V. Maheskumar, Z. Jiang, A. Du, Interfacial electronic and vacancy defect engineering coupling of the Z-scheme CsSnBr 3/SnS2 heterostructure for photovoltaic performance: a hybrid DFT study, J. Mater. Chem. A 11 (9) (2023) 4758–4768.
[19] Y. Li, J. Zhang, Q. Chen, X. Xia, M. Chen, Emerging of heterostructure materials in energy storage: a review, Adv. Mater. 33 (27) (2021) 2100855.
[20] C. Zhao, Y. Li, W. Zhang, Y. Zheng, X. Lou, B. Yu, J. Chen, Y. Chen, M. Liu, J. Wang, Heterointerface engineering for enhancing the electrochemical performance of solid oxide cells, Energ. Environ. Sci. 13 (1) (2020) 53–85.
[21] W. Li, Q. Song, M. Li, Y. Yuan, J. Zhang, N. Wang, Z. Yang, J. Huang, J. Lu, X. Li, Chemical heterointerface engineering on hybrid electrode materials for electrochemical energy storage, Small Methods 5 (8) (2021) 2100444.
[22] Y.-Y. Hsieh, H.-Y. Tuan, Architectural van der Waals Bi_2S_3/Bi_2Se_3 topological heterostructure as a superior potassium-ion storage material, Energy Stor. Mater. 51 (2022) 789–805.
[23] J. Chu, K. Han, Q. Yu, H. Wang, K. Xi, F. Lai, J. Zhang, Y. Bao, Schottky junction and multiheterostructure synergistically enhance rate performance and cycling stability, Chem. Eng. J. 430 (2022), 132994.
[24] B. Ravel, M. Newville, ATHENA, ARTEMIS, HEPHAESTUS: data analysis for X-ray absorption spectroscopy using IFEFFIT, J. Synchrotron Radiat. 12 (4) (2005) 537–541.
[25] G. Kresse, D. Joubert, From ultrasoft pseudopotentials to the projector augmented-wave method, Phys. Rev. B 59 (3) (1999) 1758–1775.
[26] J.P. Perdew, K. Burke, M. Ernzerhof, Generalized gradient approximation made simple, Phys. Rev. Lett. 77 (18) (1996) 3865–3868.
[27] S. Grimme, J. Antony, S. Ehrlich, H. Krieg, A consistent and accurate ab initio parametrization of density functional dispersion correction (DFT-D) for the 94 elements H-Pu, J. Chem. Phys. 132 (15) (2010), 154104.
[28] H.J. Monkhorst, J.D. Pack, Special points for Brillouin-zone integrations, Phys. Rev. B 13 (12) (1976) 5188–5192.
[29] A. Zhou, W. Cheng, W. Wang, Q. Zhao, J. Xie, W. Zhang, H. Gao, L. Xue, J. Li, Hexacyanoferrate-type Prussian blue analogs: principles and advances toward high-performance sodium and potassium ion batteries, Adv. Energy Mater. 11 (2) (2021) 2000943.
[30] X. Wu, Y. Ru, Y. Bai, G. Zhang, Y. Shi, H. Pang, PBA composites and their derivatives in energy and environmental applications, Coord. Chem. Rev. 451 (2022), 214260.
[31] W.-W. Shen, Y.-Y. Hsieh, H.-Y. Tuan, 3D space-confined $Co_{0.85}Se$ architecture with effective interfacial stress relaxation as anode material reveals robust and highly loading potassium-ion batteries, J. Colloid Interface Sci. 643 (2023) 626–639.
[32] H. Yu, H. Fan, X. Wu, H. Wang, Z. Luo, H. Tan, B. Yadian, Y. Huang, Q. Yan, Diffusion induced concave Co_3O_4@$CoFe_2O_4$ hollow heterostructures for high performance lithium ion battery anode, Energy Stor. Mater. 4 (2016) 145–153.
[33] B. Zhang, B. Xu, Z. Xiao, L. Cao, H. Geng, X. Ou, Inner-Stress-Dissipative, Rapid Self-Healing Core-Shell Sulfide Quantum Dots for Remarkable Potassium-Ion Storage, Energy Stor. Mater. (2023).
[34] J. Chen, A. Pan, Y. Wang, X. Cao, W. Zhang, X. Kong, Q. Su, J. Lin, G. Cao, S. Liang, Hierarchical mesoporous $MoSe_2$@CoSe/N-doped carbon nanocomposite for sodium ion batteries and hydrogen evolution reaction applications, Energy Stor. Mater. 21 (2019) 97–106.
[35] F.-W. Yuan, H.-J. Yang, H.-Y. Tuan, Seeded silicon nanowire growth catalyzed by commercially available bulk metals: broad selection of metal catalysts, superior field emission performance, and versatile nanowire/metal architectures, J. Mater. Chem. 21 (36) (2011) 13793–13800.
[36] H.-J. Yang, C.-Y. Chen, F.-W. Yuan, H.-Y. Tuan, Designed synthesis of solid and hollow $Cu_{2-x}Te$ nanocrystals with tunable near-infrared localized surface plasmon resonance, J. Phys. Chem. C 117 (42) (2013) 21955–21964.
[37] H. Shan, J. Qin, Y. Ding, H.M.K. Sari, X. Song, W. Liu, Y. Hao, J. Wang, C. Xie, J. Zhang, X. Li, Controllable heterojunctions with a semicoherent phase boundary boosting the potassium storage of $CoSe_2/FeSe_2$, Adv. Mater. 33 (37) (2021).
[38] Z. Lv, J. Fei, Y. You, X. Lv, Q. Li, J. Dang, Synergism and anion-cation dual chemical substitution in heterostructure sprouted on MXene enable high-efficiency and stable overall water splitting, J. Mater. Sci. Technol. 147 (2023) 207–216.
[39] J.H. Choi, S.K. Park, Y.C. Kang, A Salt-Templated Strategy toward Hollow Iron Selenides-Graphitic Carbon Composite Microspheres with Interconnected

Multicavities as High-Performance Anode Materials for Sodium-Ion Batteries, Small 15 (2) (2019) 1803043.
[40] L. Chen, Y. Xu, G. Cao, H.M.K. Sari, R. Duan, J. Wang, C. Xie, W. Li, X. Li, Bifunctional Catalytic Effect of CoSe2 for Lithium-Sulfur Batteries: Single Doping versus Dual Doping, Adv. Funct. Mater. 32 (8) (2022) 2107838.
[41] C.-B. Chang, Y.-R. Lu, H.-Y. Tuan, High-entropy NaCl-type metal chalcogenides as K-ion storage materials: role of the cocktail effect, Energy Stor. Mater. 59 (2023), 102770.
[42] H. Li, C. Chen, Y. Yan, T. Yan, C. Cheng, D. Sun, L. Zhang, Utilizing the Built-in Electric Field of p–n Junctions to Spatially Propel the Stepwise Polysulfide Conversion in Lithium-Sulfur Batteries, Adv. Mater. 33 (51) (2021) 2105067.
[43] A. Milbrat, R. Elbersen, R. Kas, R.M. Tiggelaar, H. Gardeniers, G. Mul, J. Huskens, Spatioselective electrochemical and photoelectrochemical functionalization of silicon microwires with axial p/n junctions, Adv. Mater. 28 (7) (2016) 1400–1405.
[44] S.-X. Yan, Q. Wang, S.-H. Luo, Y.-H. Zhang, X. Liu, Y.-G. Liu, Z.-Y. Wang, A.-M. Hao, T.-F. Yi, Coal-based S hybrid self-doped porous carbon for high-performance supercapacitors and potassium-ion batteries, J. Power Sources 461 (2020), 228151.
[45] C. Zhang, R. Du, J.J. Biendicho, M. Yi, K.e. Xiao, D. Yang, T. Zhang, X. Wang, J. Arbiol, J. Llorca, Y. Zhou, J.R. Morante, A. Cabot, Tubular CoFeP@CN as a Mott-Schottky catalyst with multiple adsorption sites for robust lithium– sulfur batteries, Adv. Energy Mater. 11 (24) (2021).
[46] X. Zhang, Y. Liu, H. Liu, T. Liang, P. Zhang, Z. Dai, $FeSe_2$/Hematite nn heterojunction with oxygen spillover for highly efficient NO_2 gas sensing, Sens. Actuators B Chem. 345 (2021), 130357.
[47] S. Ni, H. Qu, Z. Xu, X. Zhu, H. Xing, L. Wang, J. Yu, H. Liu, C. Chen, L. Yang, Interfacial engineering of the $NiSe_2$/$FeSe_2$ pp heterojunction for promoting oxygen evolution reaction and electrocatalytic urea oxidation, Appl. Catal. B 299 (2021), 120638.
[48] J. Zheng, Z. Lei, Incorporation of CoO nanoparticles in 3D marigold flower-like hierarchical architecture $MnCo_2O_4$ for highly boosting solar light photo-oxidation and reduction ability, Appl Catal B 237 (2018) 1–8.
[49] K. Jiang, B. Liu, M. Luo, S. Ning, M. Peng, Y. Zhao, Y.-R. Lu, T.-S. Chan, F.M. de Groot, Y. Tan, Single platinum atoms embedded in nanoporous cobalt selenide as electrocatalyst for accelerating hydrogen evolution reaction, Nat. Commun. 10 (1) (2019) 1743.
[50] S. Shen, Z. Wang, Z. Lin, K. Song, Q. Zhang, F. Meng, L. Gu, W. Zhong, Crystalline-amorphous interfaces coupling of CoSe2/CoP with optimized d-band center and boosted electrocatalytic hydrogen evolution, Adv. Mater. 34 (13) (2022) 2110631.
[51] S. Jiang, M. Xiang, J. Zhang, S. Chu, A. Marcelli, W. Chu, D. Wu, B. Qian, S. Tao, L. Song, Rational design of hierarchical $FeSe_2$ encapsulated with bifunctional carbon cuboids as an advanced anode for sodium-ion batteries, Nanoscale 12 (43) (2020) 22210–22216.
[52] J. Song, Y. Chen, H. Huang, J. Wang, S.-C. Huang, Y.-F. Liao, A.E. Fetohi, F. Hu, H.-y. Chen, L. Li, X. Han, K.M. El-Khatib, S. Peng, Heterointerface Engineering of Hierarchically Assembling Layered Double Hydroxides on Cobalt Selenide as Efficient Trifunctional Electrocatalysts for Water Splitting and Zinc-Air Battery, Adv. Sci. 9 (6) (2022).
[53] S.H. Yang, S.-K. Park, Y.C. Kang, MOF-derived $CoSe_2$@N-doped carbon matrix confined in hollow mesoporous carbon nanospheres as high-performance anodes for potassium-ion batteries, Nanomicro Lett 13 (2021) 1–15.
[54] S.-F. Ho, H.-Y. Tuan, Cu_3PS_4: a sulfur-rich metal phosphosulfide with superior ionic diffusion channel for high-performance potassium ion batteries/hybrid capacitors, Chem. Eng. J. 452 (2023), 139199.
[55] W. Luo, Y. Feng, D. Shen, J. Zhou, C. Gao, B. Lu, Engineering ion diffusion by CoS@SnS heterojunction for ultrahigh-rate and stable potassium batteries, ACS Appl. Mater. Interfaces 14 (14) (2022) 16379–16385.
[56] Y. Lou, P. Li, H. He, M. Zhang, In situ construction of hollow Ni_3S_2-Co_9S_8 heterostructures with enhanced reaction kinetics for potassium ion storage, J. Alloy. Compd. 937 (2023), 168249.
[57] J. Gong, R. Zhang, X. Wei, Y. Liu, Q. Luo, Q. Wan, Q. Zheng, L. Wang, S. Liu, D. Lin, Spatially dual-confined metallic selenide double active centers for boosting potassium ion storage, Chem. Eng. J. 459 (2023), 141609.
[58] L. Cao, B.i. Luo, B. Xu, J. Zhang, C. Wang, Z. Xiao, S. Li, Y. Li, B. Zhang, G. Zou, H. Hou, X. Ou, X. Ji, Stabilizing intermediate phases via efficient entrapment effects of layered VS4/SnS@C heterostructure for ultralong lifespan potassium-ion batteries, Adv. Funct. Mater. 31 (36) (2021).
[59] H. Liu, Y. He, H. Zhang, S. Wang, K. Cao, Y. Jiang, X. Liu, Q.-S. Jing, Heterostructure engineering of ultrathin SnS_2/$Ti_3C_2T_x$ nanosheets for high-performance potassium-ion batteries, J. Colloid Interface Sci. 606 (2022) 167–176.
[60] G. Suo, S. Musab Ahmed, Y. Cheng, J. Zhang, Z. Li, X. Hou, Y. Yang, X. Ye, L. Feng, L.i. Zhang, Q. Yu, Heterostructured CoS_2/$CuCo_2S_4$@ N-doped carbon hollow sphere for potassium-ion batteries, J. Colloid Interface Sci. 608 (2022) 275–283.
[61] D. Sun, C. Tang, H. Cheng, W. Xu, A. Du, H. Zhang, Pumpkin-like MoP-MoS_2@ Aspergillus niger spore-derived N-doped carbon heterostructure for enhanced potassium storage, J. Energy Chem. 72 (2022) 479–486.
[62] Y.-Y. Hsieh, K.-T. Chen, H.-Y. Tuan, A synergetic SnSb-amorphous carbon composites prepared from polyesterification process as an ultrastable potassium-ion battery anode, Chem. Eng. J. 420 (2021), 130451.
[63] X. Yang, A.L. Rogach, Electrochemical techniques in battery research: a tutorial for nonelectrochemists, Adv. Energy Mater. 9 (25) (2019) 1900747.
[64] Z. Kong, L. Wang, S. Iqbal, B. Zhang, B. Wang, J. Dou, F. Wang, Y. Qian, M. Zhang, L. Xu, Iron Selenide-Based Heterojunction Construction and Defect Engineering for Fast Potassium/Sodium-Ion Storage, Small 18 (15) (2022) 2107252.
[65] S. Kim, H. Jung, W.G. Lim, E. Lim, C. Jo, K.S. Lee, J.W. Han, J. Lee, A Versatile Strategy for Achieving Fast-Charging Batteries via Interfacial Engineering: Pseudocapacitive Potassium Storage without Nanostructuring, Small 18 (27) (2022) 2202798.
[66] W.-C. Lin, Y.-C. Yang, H.-Y. Tuan, Ternary chalcogenide anodes for high-performance potassium-ion batteries and hybrid capacitors via composition-mediated bond softening and intermediate phase, Energy Stor. Mater. 51 (2022) 38–53.
[67] Z. Zhang, X. Chen, H. Zhang, W. Liu, W. Zhu, Y. Zhu, A highly crystalline perylene imide polymer with the robust built-in electric field for efficient photocatalytic water oxidation, Adv. Mater. 32 (32) (2020) 1907746.
[68] J. Jing, J. Yang, Z. Zhang, Y. Zhu, Supramolecular zinc porphyrin photocatalyst with strong reduction ability and robust built-in electric field for highly efficient hydrogen production, Adv. Energy Mater. 11 (29) (2021) 2101392.
[69] T. Wang, J. Zhao, L. Qi, G. Li, W. Yang, Y. Li, Ultrathin graphdiyne oxide-intercalated MXene: A new heterostructure with interfacial synergistic effect for high performance lithium-ion storage, Energy Stor. Mater. 54 (2023) 10–19.
[70] M. Li, X. Pan, M. Jiang, Y. Zhang, Y. Tang, G. Fu, Interface engineering of oxygen-vacancy-rich CoP/CeO_2 heterostructure boosts oxygen evolution reaction, Chem. Eng. J. 395 (2020), 125160.
[71] J. Li, Y. Kang, Z. Lei, P. Liu, Well-controlled 3D flower-like CoP_3/CeO_2/C heterostructures as bifunctional oxygen electrocatalysts for rechargeable Zn-air batteries, Appl. Catal. B 321 (2023), 122029.
[72] X. Yun, T. Lu, R. Zhou, Z. Lu, J. Li, Y. Zhu, Heterostructured $NiSe_2$/$CoSe_2$ hollow microspheres as battery-type cathode for hybrid supercapacitors: Electrochemical kinetics and energy storage mechanism, Chem. Eng. J. 426 (2021), 131328.
[73] B. Pandit, S.R. Rondiya, S. Shegokar, L.K. Bommineedi, R.W. Cross, N.Y. Dzade, B. R. Sankapal, Combined electrochemical and DFT investigations of iron selenide: a mechanically bendable solid-state symmetric supercapacitor, Sustain. Energy Fuels 5 (19) (2021) 5001–5012.
[74] X. Huang, J. Sun, L. Wang, X. Tong, S.X. Dou, Z.M. Wang, Advanced high-performance potassium–chalcogen (S, Se, Te) batteries, Small 17 (6) (2021) 2004369.
[75] C.-H. Chang, K.-T. Chen, Y.-Y. Hsieh, C.-B. Chang, H.-Y. Tuan, Crystal facet and architecture engineering of metal oxide nanonetwork anodes for high-performance potassium ion batteries and hybrid capacitors, ACS Nano 16 (1) (2022) 1486–1501.
[76] Z. Wang, K. Dong, D. Wang, F. Chen, S. Luo, Y. Liu, C. He, C. Shi, N. Zhao, Monodisperse multicore-shell SnSb@SnO_x/SbO_x@C nanoparticles space-confined in 3D porous carbon networks as high-performance anode for Li-ion and Na-ion batteries, Chem. Eng. J. 371 (2019) 356–365.
[77] Z. Wang, K. Dong, D. Wang, S. Luo, Y. Liu, Q. Wang, Y. Zhang, A. Hao, C. Shi, N. Zhao, A nanosized SnSb alloy confined in N-doped 3D porous carbon coupled with ether-based electrolytes toward high-performance potassium-ion batteries, J. Mater. Chem. A 7 (23) (2019) 14309–14318.
[78] X.-F. Wu, Z.-J. Li, J.-X. Liu, W. Luo, J.-J. Gaumet, L.-Q. Mai, Defect engineering of hierarchical porous carbon microspheres for potassium-ion storage, Rare Met. 41 (10) (2022) 3446–3455.